Spring 2014

No And No2 Modeling For Diesel Oxidation Catalyst At Different Thermal Aging Levels

Keqin Zhou
Purdue University

Graduate School ETD Form 9
(Revised 01/14)

PURDUE UNIVERSITY
GRADUATE SCHOOL
Thesis/Dissertation Acceptance

This is to certify that the thesis/dissertation prepared

By Keqin Zhou

Entitled
NO AND NO2 MODELING FOR DIESEL OXIDATION CATALYST AT DIFFERENT THERMAL AGING LEVELS.

For the degree of Master of Science in Engineering

Is approved by the final examining committee:

Peter H. Meckl

Galen B. King

Gregory M. Shaver

To the best of my knowledge and as understood by the student in the *Thesis/Dissertation Agreement. Publication Delay, and Certification/Disclaimer (Graduate School Form 32)*, this thesis/dissertation adheres to the provisions of Purdue University's "Policy on Integrity in Research" and the use of copyrighted material.

Peter H. Meckl

Approved by Major Professor(s): _____

_____

Approved by: David C. Anderson 04/23/2014

Head of the Department Graduate Program Date

NO AND NO_2 MODELING FOR DIESEL OXIDATION CATALYST AT DIFFERENT THERMAL AGING LEVELS

A Thesis

Submitted to the Faculty

of

Purdue University

by

Keqin Zhou

In Partial Fulfillment of the

Requirements for the Degree

of

Master of Science in Engineering

May 2014

Purdue University

West Lafayette, Indiana

ACKNOWLEDGEMENTS

I would like to give my most sincere gratitude to my advisor Dr. Meckl for guiding me through my research work during the past two years and never giving up on me regardless of the obstacles I confronted during research. I would like to give my genuine thanks to my parents who are always behind me and give me mental support. I would like to thank my research partner Prateek Tayal for cooperating with me in engine testing; experiments wouldn't have been so efficient without his patient troubleshooting and communication with technicians at CAMBUSTION. I want to give special thanks to Jagdish who has been very generous in helping me out in GT-Power, engine performance and design of experiments. I would also like to thank Kyle Wright for providing thermal aging service free of charge at Alcoa in Lafayette. I would like to thank all my friends and Herrick Lab shop guys for providing all kinds of support when I got stuck somewhere, I have no space to list them all, but I appreciate very much their company and support, and I will graduate from Herrick lab with such cooperative and obliging spirit engraved on my mind.

TABLE OF CONTENTS

Page

LIST OF TABLES

LIST OF FIGURES

Figure Page

Figure Page

Figure Page

ABSTRACT

Zhou, Keqin. M.S.E., Purdue University, May 2014. NO and NO_2 Modeling for Diesel Oxidation Catalyst at Different Thermal Aging Levels. Major Professor: Peter H. Meckl, School of Mechanical Engineering.

Different DOC modeling methods are analyzed and compared. Detailed reaction mechanisms of DOC reaction are discussed and a new NO and NO_2 modeling technique is proposed. Experiments are conducted measuring downstream DOC NO and NOx. DOC out NO and NO_2 concentrations are modeled as a function of DOC temperature. A robust model is built such that with the input of real time NO_x and DOC temperature information, DOC-out NO and NO_2 concentrations can be precisely predicted.

As is true with many catalysts, the DOC thermally ages as it operates, which reduces the thermal effectiveness level of the catalyst. This directly reduces the amount of HC, CO and NO it is able to oxidize, increasing the DOC-out NO percentage. In this thesis, aged DOC model is recalibrated in modeling DOC-out NO and NO_2 concentrations. Correlations between HC light-off temperature shift and DOC-out NO and NO_2 concentration shift are discovered and analyzed. A preliminary model of NO and NO_2 concentrations as a function of HC light-off temperature and DOC temperature is built and validated against actual data.

CHAPTER 1. INTRODUCTION

1.1 Introduction

For many years, diesel engines have been used in most industrial sectors overwhelmingly because they provide more power per unit of fuel and diesel fuel's lower volatility makes it safer to handle. Diesel engine generators bring clean and affordable standby power within the reach of millions of enterprises, homes and small businesses. Diesel engines have occupied a majority of modern heavy road vehicles like trucks and buses, ships, long-distance trains, and most farm and mining vehicles. The newer automotive diesel engines have power-weight ratios comparable to spark-ignition designs and have far superior fuel efficiency. The largest diesel engines are popular among power ships and liners along the high seas. Hundreds of applications have proven the fact that diesel engines are gaining importance in construction, transportation as well as military usage.

Despite the merits of diesel engine, the comparatively high combustion temperature results in more emission problems such as soot and NO_x. On December 21, 2000 the EPA released emission standards for model year 2007 and later heavy-duty highway engines (the California ARB adopted virtually identical 2007 heavy-duty engine standards in October 2001). With regards to the emission standards, regulation introduces new, very stringent emission standards, as follows: PM 0.01 g/bhp-hr, NO_x

0.20 g/bhp-hr, NMHC 0.14 g/bhp-hr. The emission regulations regarding to nonroad diesel engine emission standard table is listed in Table 1.1 [1].

Table 1.1. EPA Tire 1-3 Nonroad diesel engine emission standards, g/k Wh [1].

Rated Power (kW)	Tier	Model Year	NMHC (g/kW-hr)	NMHC + NO_x (g/kW-hr)	NO_x (g/kW-hr)	PM (g/kW-hr)	CO (g/kW-hr)
kW < 8	1	2000-2004	-	10.5	-	1.0	8.0
	2	2005-2007	-	7.5	-	0.80	8.0
8 ≤ kW < 19	1	2000-2004	-	9.5	-	0.80	6.6
	2	2005-2007	-	7.5	-	0.80	6.6
19 ≤ kW < 37	1	1999-2003	-	9.5	-	0.80	5.5
	2	2004-2007	-	7.5	-	0.60	5.5
37 ≤ kW < 56	1	1998-2003	-	-	9.2	-	-
	2	2004-2007	-	7.5	-	0.40	5.0
	3[f]	2008-2011	-	4.7	-	0.40	5.0
56 ≤ kW < 75	1	1998-2003	-	-	9.2	-	-
	2	2004-2007	-	7.5	-	0.40	5.0
	3	2008-2011	-	4.7	-	0.40	5.0
75 ≤ kW < 130	1	1997-2002	-	-	9.2	-	-
	2	2003-2006	-	6.6	-	0.30	5.0
	3	2007-2011	-	4.0	-	0.30	5.0
130 ≤ kW < 225	1	1996-2002	1.3[j]	-	9.2	0.54	11.4
	2	2003-2005	-	6.6	-	0.20	3.5
	3	2006-2010	-	4.0	-	0.20	3.5
225 ≤ kW < 450	1	1996-2000	1.3j	-	9.2	0.54	11.4
	2	2001-2005	-	6.4	-	0.20	3.5
	3	2006-2010	-	4.0	-	0.20	3.5
450 ≤ kW < 560	1	1996-2001	1.3[j]	-	9.2	0.54	11.4
	2	2002-2005	-	6.4	-	0.20	3.5
	3	2006-2010	-	4.0	-	0.20	3.5

Table 1.1. Continued.

560 ≤ kW< 900	1	2000-2005	1.3j	-	9.2	0.54	11.4
	2	2006-2010	-	6.4	-	0.20	3.5
kW > 900	1	2000-2005	1.3j	-	9.2	0.54	11.4
	2	2006-2010	-	6.4	-	0.20	3.5

At the same time, diesel engine manufactures like Cummins, Ford and John Deere continuously improve their engine aftertreatment technologies. NO_x control developments on selective catalytic reduction (SCR), lean NO_x traps (LNT) and lean NO_x catalysts (LNC) were developed rapidly to capture the soot as well as reduce the NMHC, CO, and NO_x. It has been reported that DLB-FT (diesel particulate filters) can remove over 90% of the exhaust particulate emissions [2-4].

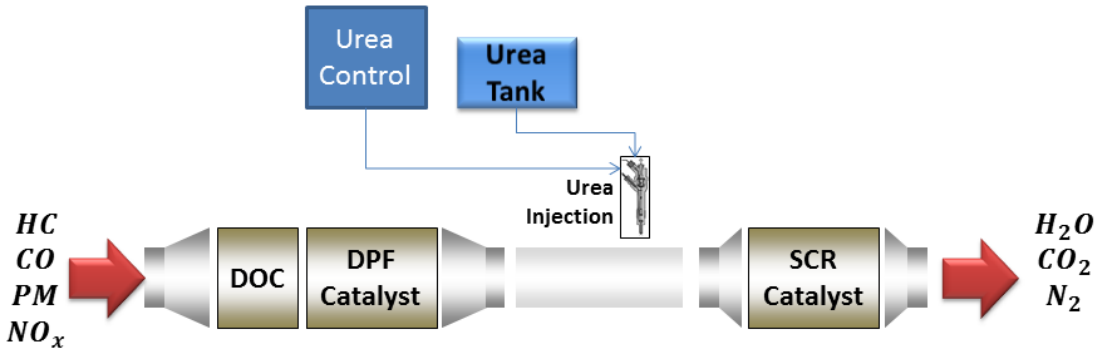

Figure 1.1. Emission system of heavy duty diesel engine.

As we can see from Figure 1.1, a heavy duty diesel engine usually has an emission system that includes DOC (diesel oxidation catalyst), DLB-FT (diesel particulate filter) and SCR (selective catalytic reactor). DOC is mainly responsible for oxidation of pollutant. It oxidizes hydrocarbons and carbon monoxide in the exhaust stream into H_2O and CO_2, which are environmentally friendly. It is also responsible for oxidizing engine out NO into NO_2. After the process of DOC, the emission flow goes

through DLB-FT, which captures and burns the soot, in turn reduces PM (particulate matter) level of emission. At this point, emission gas still has unburned NO and NO_2, which will be further processed through SCR by urea (active ingredient is ammonia) dosing and finally convert NO_x into nitrogen and water.

Like many other catalysts, DOC deactivates as the usage increases. The deactivation occurs in the form of chemical, thermal, and mechanical charges, which will be discussed further in Chapter 2. The most common deactivation form is thermal aging, which reduces the effective surface area of the catalyst and in turn reduces the ability for oxidation, especially the oxidation of NO due to the catalyst selectivity. NO/NO_2 is considered a critical factor affecting theoretical urea dosing amount in the SCR process. Thus, technique that could estimate the aging level of DOC is of great importance such that DOC out NO and NO_2 concentration could be estimated, which further enables proper urea dosing downstream of the DOC in the SCR system.

An easy and feasible method of detecting the thermal aging level of DOC would be through the detection of light-off temperature. Light-off temperature is the temperature at which the chemical reaction rate passes 50%, which is considered the temperature at which the catalyst starts functioning. Researchers have discovered that the light-off temperature increases with thermal aging of catalyst [5-6]. This thesis aims to develop a model of DOC that uses effective surface area as a function of light-off temperature to estimate DOC-out NO and NO_2 concentration.

This thesis is composed of 5 chapters, which includes the introduction chapter, Chapter 2 presents background information on DOC (diesel oxidation catalyst) fundamentals, how aging affects the DOC, and a literature review section of previous

research regarding modeling of aftertreatment systems of diesel engines. Chapter 3 presents the introduction of the model as well as calibration to the experimental data. Chapter 4 presents the test set-up for experimental calibration and experimental results analysis. Engine, DOC, and test cell instrumentation specifications are presented in this Chapter. Chapter 5 presents the conclusion of this research and provides recommendations for future research.

CHAPTER 2. BACKGROUND AND LITERATURE REVIEW

This chapter provides fundamentals on diesel engines, diesel oxidation catalysts and aging, which provides a brief introduction. Previous research in modeling diesel oxidation catalysts since the early 1980s is reviewed. CI engine fundamentals are presented in section 2.1. Configurations of the engine aftertreatment system is presented in section 2.2. DOC structures and knowledge is explained in section 2.3. Light-off temperature and its shift is discussed in section 2.4. Catalyst deactivation knowledge is explained in section 2.5. References of DOC modeling are discussed in detail in section 2.6. Models are compared regarding different methods. Section 2.7 talks about on board diagnostics and how it comes to the picture and its application.

2.1 Brief Introduction about CI Engine

As a type of IC engine (internal combustion engine), the ignition method of CI engine (compression-ignition engine) is through compression heat to reach ignition temperature. The fuel injected into the combustion chamber is then burned. In contrast to CI engines, SI engines require a spark plug so that the air-fuel mixture can be ignited.

The biggest advantage of a CI engine is its high thermal efficiency, because of its comparatively higher compression ratio. A high compression ratio is desirable because available oxygen and fuel molecules are placed into a reduced space along with the adiabatic heat of compression, which will result in better mixing and evaporation of the

fuel. This not only increases the power generated at the moment, but also increases the useful work extracted from the power by the expansion of hot fuel. However, a high compression ratio can't be applied to SI engines because it causes knocking, especially when low octane fuel is used. This not only reduces the efficiency of the engine but also causes severe damage to the engine.

CI engines are manufactured in two-stroke and four-stroke versions. The original intuition for the CI engine was to replace stationary steam engines because of its higher efficiency. In 1885, Herbert Akroyd Stuart from England investigated the possibility of using paraffin oil (prototype of diesel) for an engine. Built in 1891, his engine was the first internal combustion engine using a pressurized fuel injection system [7]. However, the compression ratio Stuart used was not high enough to initiate ignition. To fix this, combustion took place in a separated combustion chamber called a 'vaporizer' which was mounted on the head of the cylinder. Self-ignition occurred from contact between the fuel-air mixture and the hot walls of the vaporizer [8]. The temperature of the vaporizer increased as engine torque increased, which resulted in early ignition. The design of the mechanism required that water was dripped into the air intake to cancel out pre-ignition [9]. There were certain issues with the initial CI engine, however, the revolutionary idea of direct fuel injection and compression-ignition were of great influence in the future, which were patented by Stuart and Charles Binney in May 1890 [10]. However, at that time Stuart's engine still requires the supplement of heat to the cylinder during engine cold start. By 1892, Stuart overcame this issue and produced engine without requirement of heat source [11]. In the 1910s, the CI engine had started being introduced to ships, followed by heavy equipment, locomotives and trucks. It was not until 1930s that the CI

engine was introduced to the automobiles industry, which witnessed a drastic increase since the 1970s.

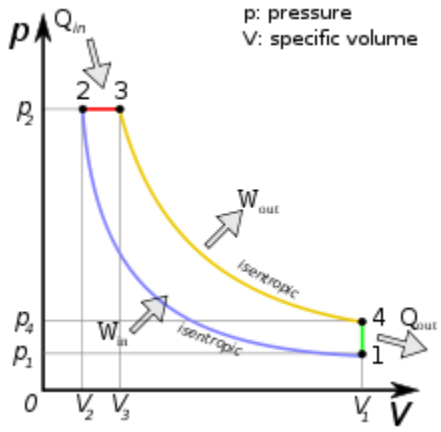

Figure 2.1. p-V diagram of a 4 stroke slow stroke diesel engine.

An ideal 4-stroke diesel engine works as shown in the pressure-volume diagram in Figure 2.1 here in a clockwise direction from 1 to 4. The first stroke is the intake stroke, during which the piston begins at the top dead center. The piston slowly departs the top while the volume of cylinder keeps increasing, introducing air into the combustion chamber. This movement ends when the piston reaches the bottom. The second stroke is named the compression stroke when the piston goes back to the top of the cylinder, when fuel is injected directly into the compressed air in the combustion chamber. While intake and exhaust valves are both closed, fuel-air mixture get compressed in a ratio between 15:1 to 22:1. Compression heat can be as high as 1022 K during this process. The third stroke is ignition. It starts when the piston is at the top dead center and ignition is initiated because of the heat of compression. As a result of combustion, the compressed fuel-air mixture pushes the piston down to the bottom center. In the fourth stroke, the piston returns to the top center while the exhaust valve is opened. This stroke enables the outlet

of the exhaust, which contains unburned hydrocarbon, carbon monoxide, PM (particular matter) as well as NO_x, which will be further processed by the aftertreatment system of the diesel engine.

2.2 Configuration of Aftertreatment System

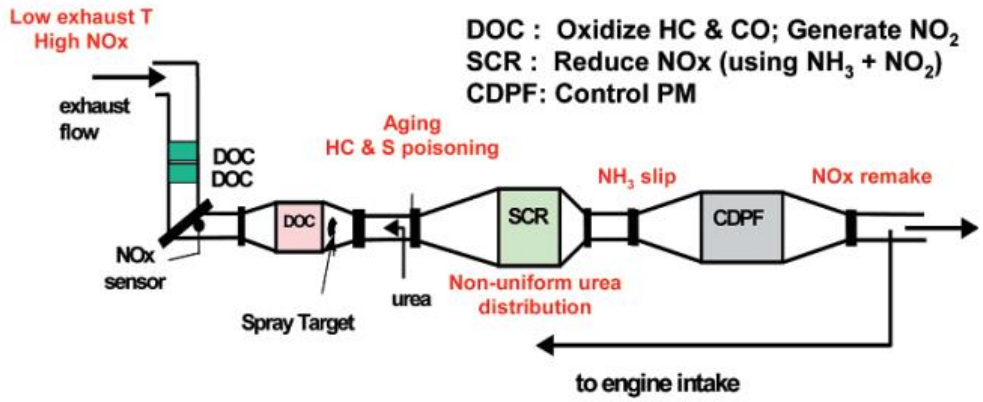

Figure 2.2. Aftertreatment configuration of heavy duty diesel engine [12].

Catalytic converter usually refers to equipment that processes toxic vehicle emissions so that they meet the regulatory requirements. The process of catalytic conversion is usually oxidation or reduction. The applications of catalytic converters are mainly on diesel or gasoline engines. As a result of the U.S. Environmental Protection Agency's stricter regulation of exhaust emissions [13][14][15][16]. 'Two way' gasoline catalytic converters were first invented and manufactured during 1975. These catalytic converters are responsible for converting unburned hydrocarbon and carbon monoxide into water and carbon dioxide. In 1981, gasoline catalytic converters were upgraded into 'three way catalyst', which further reduce unburned NO_x into nitrogen and water. Nowadays, three-way converters are still used in gasoline engines and two-way converters are still equipped in lean engines.

For CI engine (compression ignition engine), different applications of catalytic converters have been developed. DOC (diesel oxidation catalyst) is the most commonly used catalytic converter. Similar to the function of 'two way catalyst' in gasoline engine emission system, the function of DOC is also to oxidize carbon monoxide as well as unburned hydrocarbon. However, DOC alone will not reduce the amount of NO_x in the pollutant. Two techniques have been developed regarding this issue. The first one is the NO_x absorber, which contains precious metal that captures NO_x. The second one, which is more widely accepted and manufactured, is SCR (selective catalytic reduction). Regulations announced that diesel engines built after 2007 require DLB-FT (diesel particulate filter) for soot capture [17].

2.3 DOC Basics

As shown in Figure 2.3, DOC structures as a flow-through ceramic monolith with washcoat of catalytic metals. Exhaust gas enters the monolith through one end and flows through the DOC, oxidizing NO, CO, and HC. The substrate of the DOC is usually ceramic as the material needs to handle high temperature and high temperature gradient. Washcoat material is Al_2O_3 as referred from other publications [18-19].

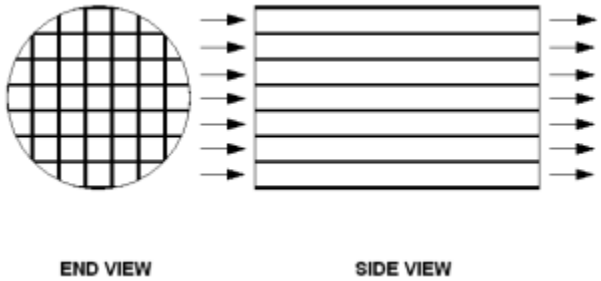

Figure 2.3. End view and Side view of DOC [20].

The placement of the DOC was originally well downstream of the engine due to the varying applications of the same diesel powertrain [21]. However, this placement causes problems for the catalytic reaction in the DOC, which was shown to have higher reaction rates at higher temperatures in certain temperature range [22, 23]. As shown in Figure 2.4, at temperatures less than 150 °C, the catalyst shows low activity, resulting in low conversion rates. When temperature exceeds 250 °C, HC conversion rate passes 50%, when temperature reaches 300 C, the efficiency is at maximum and stops increasing as temperature increases. More emissions constituents are able to slip past the catalyst at lower temperature (for instance, during a cold start), so maximizing the DOC's low temperature oxidation capability was a must for designers [22].

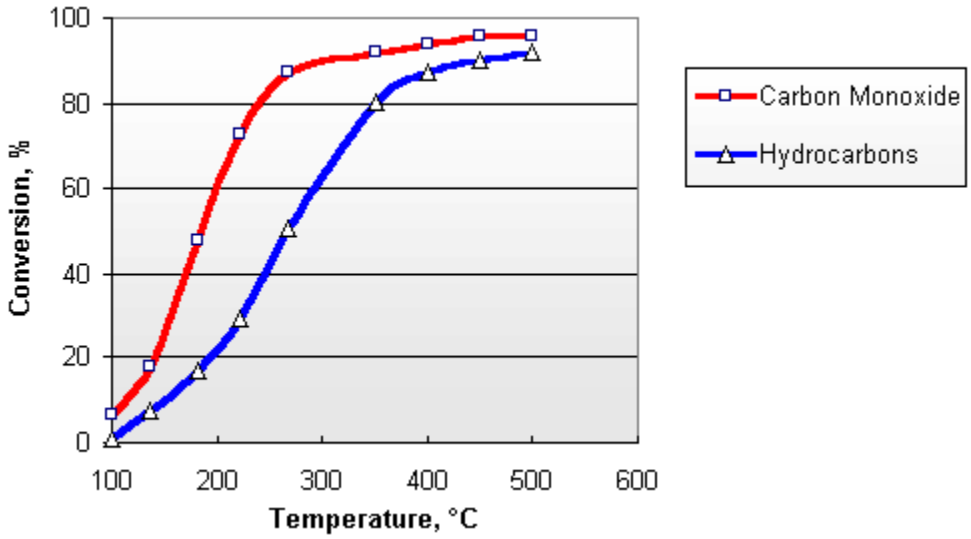

Figure 2.4. Conversion rate of DOC at different temperatures [20].

2.4 Basics of Light-off Temperature and Its Shift

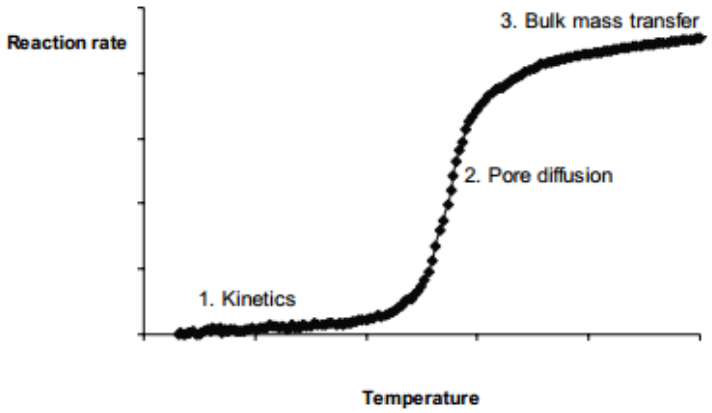

Figure 2.5. Different phase of reaction [24].

Catalyst light-off temperature is the temperature of the reaction when it passes 50% conversion. This temperature acts as indicator of effectiveness level of vehicle emission catalyst: the lower the light-off temperature, the fresher and more effective the catalyst is. Usually the catalyst reaction follows the trend shown in Figure 2.5. When temperature is low, the reaction rate is very low and there is almost no conversion on the surface of the catalyst. At this point, the rate-determining step which controls the speed of reaction is the reaction kinetics. Since the temperature is not high enough to overcome the energy barrier, the kinetics is extremely low. Second stage of reaction is during a very small temperature range when the conversion rate ramps up as shown in Figure 2.6. At this time, the rate-determining step which limits the reaction from being even faster is the solid phase pore diffusion rate. Detailed diffusion and mass transfer will be discussed in section 2.5 regarding the heterogeneous catalysis. Light-off happens at this stage, and temperature is high enough not to limit the chemical kinetics. When the temperature is higher, the reaction reaches the third stage. The limit of this stage is due to the bulk mass transfer between the solid phase and gas phase. In this case, reactions are restricted

thermodynamically because oxidation reactions are exothermic. At this point, even if the temperature gets higher there wouldn't be a big increase in reaction rate.

With regards to the deactivation of catalyst, researches have proved that light-off temperature shifts higher as the DOC ages. (See Figure 2.6 [24] A) H2/800°C/3h-aged; B) air/800°C/3h-aged; C) H2/1000°C/3h-aged; D) H2/1200°C/3h-aged E) air/1000°C/3h-aged, and F) air/1200°C/3h-aged; lean reaction conditions [24].) Aging procedures has been performed and the light-off temperature of CO has shifted from 130 C to 270 C.

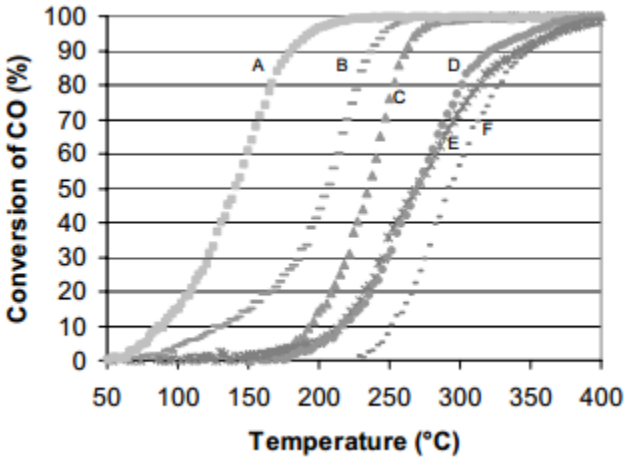

Figure 2.6. Comparison of light-off temperature shift [24].

2.5 Deactivation of Catalyst

When the DOC is fresh, the microstructure looks similar to Figure 2.8. This shows how the catalyst substrate is shaped, and how the nano-scaled precious platinum particle is scattered on the surface of the Al2O3 washcoat. High surface areas as well as extra small metal particles enable high specific surface area of the precious metal. The reaction conversion rate is best when the catalyst is fresh. Figure 2.7 shows pictures of the DOC in fresh and aged conditions. From the picture, it can be seen that the scattered PGM sites on the left side of the picture have been agglomerated into a much bigger size.

This will result in a smaller specific surface area, which will result in the reduction of effectiveness level in oxidizing pollutant.

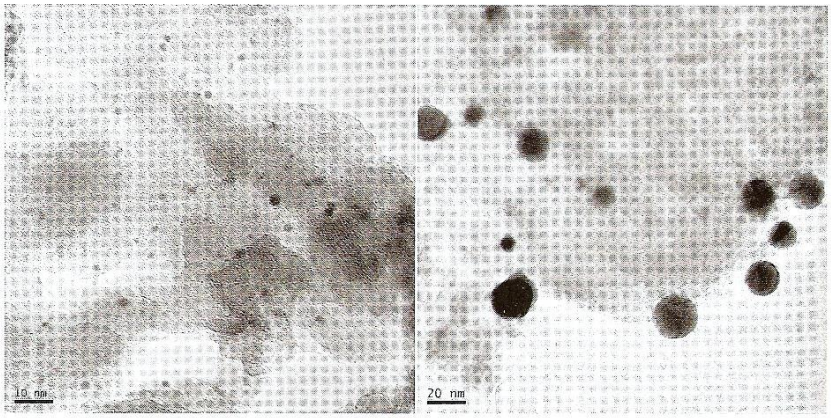

Figure 2.7. Decay by sintering resulting in agglomeration of deposited metal sites [25].

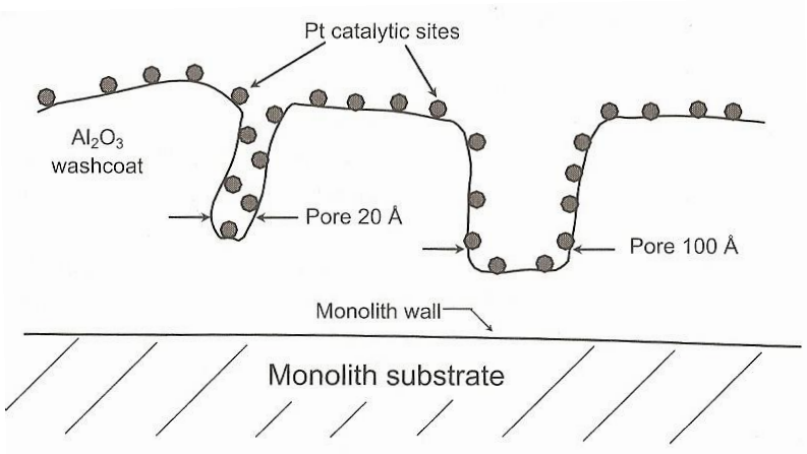

Figure 2.8. Conceptual model of fresh DOC catalyst [6].

Catalyst deactivation is a phenomenon in which the micro structure changes, which leads to the loss of active sites. The macro change is directly reflected in the performance of the catalyst. The deactivation is a slow, inevitable process. There are various forms of deactivation shown in Table 2.1.

Table 2.1. Various forms of deactivation [24].

Thermal	Chemical	Fouling	Mechanical
Sintering	Poisoning: irreversible adsorption or reaction on/with the surface	Coke formation (carbon deposits)	Thermal shock
Alloying	Inhibition: competive reversible adsorption of poison precursors		Attrition
Support changes	Poison-induced reconstruction of catalytic surfaces		Physical breakage
Precious metal-base metal interactions	Physical/chemical blockage of support pore structure		
Metal/metal oxide-support interactions			
Oxidation			
Precious metal surface orientation			
Metal volatilization			

Among all four categories of deactivation, the most common ones are thermal sintering, chemical poisoning and coke formation. Usually the deactivation mechanisms don't occur separately. Aging in a DOC appears to be a combination of the mechanisms. Whichever the mechanism is, they all result in the loss of active surface area, which in turn reduces the reaction conversion performance.

Thermal degradation, which is usually called thermal aging, is considered the main cause of aging in vehicle emission catalysts. Consecutive running under high temperature is known to have an impact on the effectiveness level of three-way catalysts [26]. When seen in a microscope, the high temperature causes precious metal to agglomerate, which lowers the specific surface area as shown in Figure 2.9. Figure 2.10 here shows the high temperature causes sintering and solid-solid phase transitions of the washcoat and encapsulation of active metal particles [27].

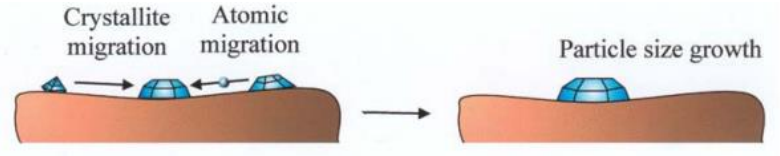

Figure 2.9. Precious metal growth [24].

Figure 2.10. Sintering process of substrate [24].

Sintering on the catalyst support is a complex phenomenon that involves chemical and physical change. To understand the mechanism of change might require a good amount of research regarding material science. Research has proved sintering is strongly exponentially dependent on temperature [28]. Surrounding environment and atmosphere can also affect the process of sintering [29]. Research has proved that water vapor environment strongly speeds up sintering process [30]. This explains why researchers simulate the aging process by putting DOC inside a heated oven with water vapor inside to accelerate the sintering process.

2.6 Basics and References of DOC Reactions and Modeling

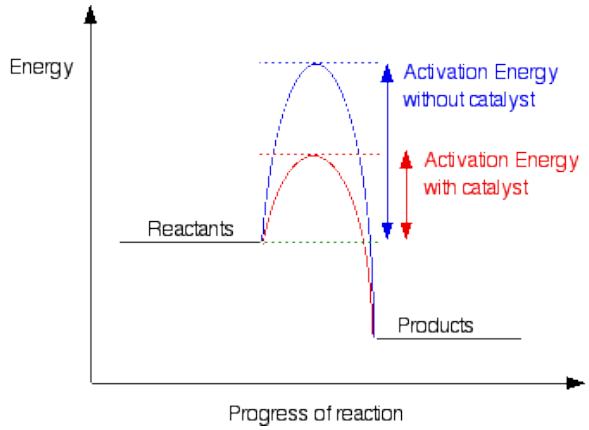

Figure 2.11. Reaction process with and without catalyst [20].

Padilla [20] developed a transient model for DOC and DPF. The reaction in the DOC is described as heterogeneous catalyst reaction. In chemistry, heterogeneous catalysis refers to the form of catalysis where the phase of the catalyst differs from that of the reactants [32]. Reactants of CO, NOx, and HC are in gas phase, however, catalyst oxidation reaction happens in the solid phase rather than the gas phase, which requires phase transformation. This is because the gas phase reaction requires a much higher activation energy, while the catalyst enables the reaction to happen at comparatively lower energy barrier, as shown in Figure 2.11. The reaction favors the path with the lower energy barrier, in this case through the catalyst reaction. Specifically, in a DOC there are 5 classified processes involved in the reaction. They are:

1. Diffusion of reactants;
2. Adsorption of reactants;
3. Catalytic reactions;
4. Desorption of products;
5. Diffusion of products.

During the first process, the reactants first diffuse through a gas boundary layer and land on catalytic sites (Al2O3 surface). Then the molecules of reactants further diffuse through a porous carrier towards dispersed active sites (Pt active particles). Secondly, molecules need to go through the adsorption process during which reaction molecules tightly bond with solid phase effective sites. Thirdly is the catalytic reaction during which reactants are converted into products. Fourth step is the desorption step when products molecules desorb from the catalytic sites. Finally, diffusion happens and the product molecules return to the gas phase and flow downstream for further processing.

Figure 2.12 shows the structure of the model. This model is able to calibrate and model the DOC out HC, CO, and NO concentrations. However, the calibration process for this model is very complicated. It requires the calibration of diffusion between solid phase and gas phase requires temperature programed desorption experiment. The reaction rate of each species requires upstream, downstream DOC HC, NO, and CO measurements. Also, the inhibition factor for different species is highly empirical and varies from set points. On top of the problems discussed above, the model only works for a fresh DOC, which means when the DOC ages, the model will require recalibration before predicting DOC-out concentration precisely. Solving ten coupled partial differential equations takes time so that it might cause difficulty in predicting real-time DOC out concentration without time delay.

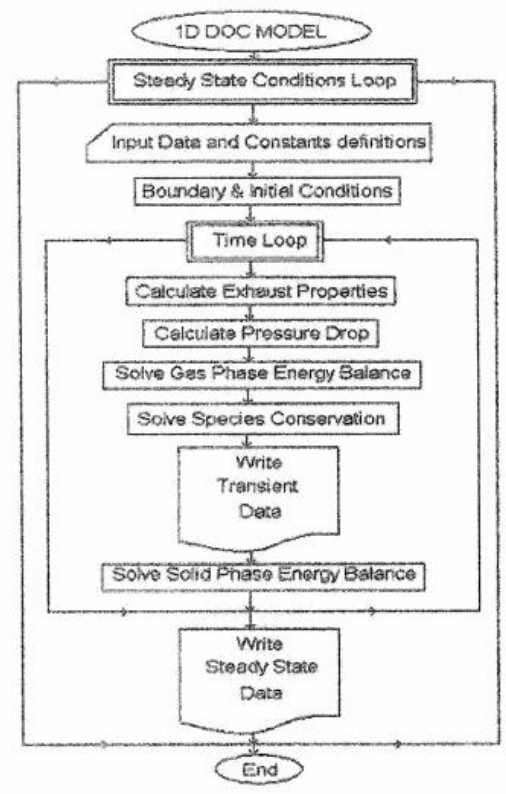

Figure 2.12. DOC code structure flow diagram [20].

Hsieh [36] developed an observer-based estimation that is able to predict downstream NO and NO_2 concentrations. Hsieh first developed engine out NO_2 and NO_x relations so that with only a NO_x sensor, upstream NO and NO_2 concentration can be predicted as shown in Figure 2.13.

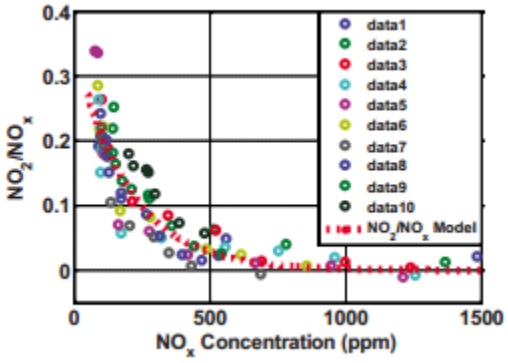

Figure 2.13. Experimental fitting of engine out NO_2 and NO_x [36].

Based on the above assumptions, the NO/NO_2 dynamics inside a DOC can be explained by the forward and reverse reactions of Eq. (2.1):

$$NO + \frac{1}{2}O_2 \overset{DOC\ catalyst}{\longleftrightarrow} NO_2. \tag{2.1}$$

NO concentration dynamics is modeled in CSTR reactor model shown in Eq. (2.2):

$$\dot{C}_{NO,DOC} = \frac{F_{in}}{V_{DOC}}\left(C_{NO,in} - C_{NO,DOC}\frac{T_{DOC}}{T_{in}}\right) - \frac{R_{oxi}}{V_{DOC}} + \frac{R_{red}}{V_{DOC}}. \tag{2.2}$$

The reaction rates can be modeled by the modified Arrhenius equation, where R_{oxi} is the reaction rate of Eq. (2.3):

$$R_{oxi} = k_{oxi}{T_{DOC}}^{\alpha_{oxi}} e^{-(E_{oxi}/RT_{DOC})^{\beta_{oxi}}} C_{NO,DOC} C_{O_2,DOC} \tag{2.3}$$

in the forward direction (oxidation), R_{red} is the reaction rate of Eq. (2.4):

$$R_{red} = k_{red}{T_{DOC}}^{\alpha_{red}} e^{-(E_{red}/RT_{DOC})^{\beta_{red}}} C_{NO_2,DOC} \tag{2.4}$$

in the reverse direction (NO_2 reduction); α_{oxi}, α_{red}, β_{oxi}, β_{red}, k_{oxi}, k_{red} , E_{oxi}, E_{red}, and R are positive constants that require calibration; C_{NO}, C_{NO2}, and C_{O2} are mole concentrations of NO, NO_2, and O_2; and T_{DOC} is the DOC temperature. CSTR model is then applied to this model with the input of DOC temperature and flow rate. This model used genetic algorithm in optimizing parameters.

However, I was not able to apply this approach to my research as my experimental engine-out NO_2/NO_x fails to show correlation with NO_x concentration. Also, CSTR reactor (continuous stirred tank reactor) model might not be as accurate in modeling DOC as compared to plug flow reactor. At low temperature, the reaction is usually not able to reach equilibrium, which is the prerequisite of CSTR reactor. Also, the aged DOC will require recalibration for parameters in this model.

Katare [37] developed a mathematical algorithm for nonlinear aftertreatment model. In his research, he used nonlinear curve fitting applied to downstream DOC HC, NO and CO concentration. He discovered that NO conversion through DOC can be modeled as a Weibull distribution.

Figure 2.14 shows the model fitting of conversion of NO into NO_2. From this figure, we are able to see that NO oxidation can be precisely captured. However, this is only the conversion curve. In order to get the downstream DOC NO and NO_2 concentrations, it still requires input of upstream NO and NO_2 concentration.

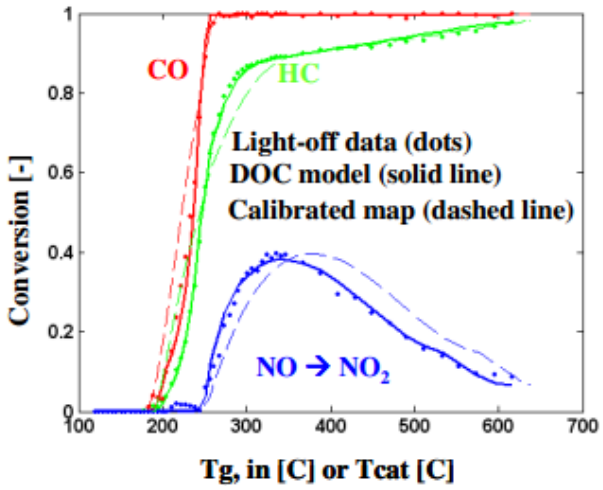

Figure 2.14. Results from calibration of HC, CO and NO conversion rate [37].

2.7 DOC-out NO and NO_2 Concentration Application

The "standard" SCR equation is given in the form of

$$4NH_3{}^* + 4NO + O_2 \xrightarrow{Catalyst} 4N_2 + 6H_2O, \tag{2.5}$$

since the reaction rate is fast and NO_x normally consists of more NO than NO_2. The following equation,

$$2NH_3{}^* + NO + NO_2 \xrightarrow{Catalyst} 2N_2 + 3H_2O, \tag{2.6}$$

is called "fast SCR", because the reaction rate can be one order of magnitude faster than the standard SCR reaction, as studied in [38][39].

The goal of this research project is based on the following two background ideas. First is the knowledge that previous studies showed that NO/NO_2 ratio in diesel engines could be modeled as a function of catalyst temperature as shown in Figure 2.15, so that with the already available NO_x sensor in every diesel truck, additional NO and NO_2 concentrations will be available to better predict the SCR urea dosing input. Second is the idea of light-off temperature. Researchers have discovered that catalyst effectiveness

level can be determined as a function of light-off temperature. When light-off temperature is taken as an additional term or axis, a 3-D model can be built which has the x-axis of catalyst temperature, y-axis of light-off temperature, z-axis of conversion related parameter.

When Kp can be modelled as a function of DOC temperature and HC light-off temperature, real-time NO and NO_2 concentrations can be calculated at any time, and the DOC-out NO and NO_2 concentration modeling will help SCR in urea dosing amount calculation.

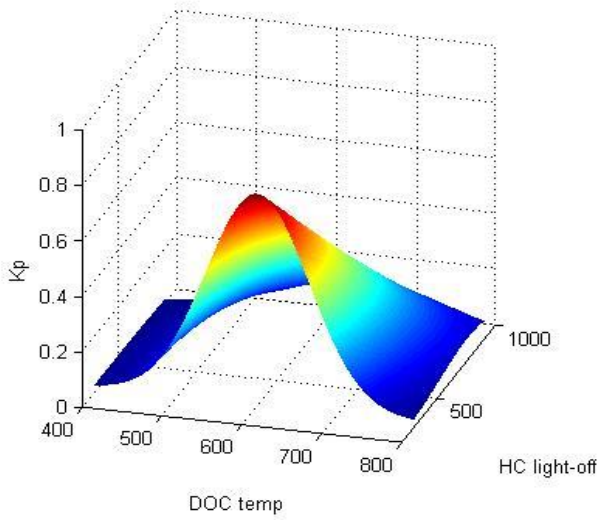

Figure 2.15. Assumption of a 3-D model featuring DOC temperature and HC light-off temperature.

CHAPTER 3. EXPERIMENTATION AND ANALYSIS

3.1 Experimental Procedures and Test Set-up

This chapter explains the experimental setup including the critical equipment such as engine, dynamometer, analyzers and aftertreatment system. Hardware plays a very important role in modeling as it enables experiments as well as accurate data results.

The engine used in this project is located in Ray W. Herrick Laboratory. This Cummins ISB 6.7 L engine is equipped with EGR system, variable geometry turbocharger, and emission piping system. Table 3.1 lists the engine configuration. In this project specifically, the engine serves as input that provides real time feed gas into the aftertreatment system. The advantage of using a real engine instead of synthesized gas bench is the gas components are real, which makes the model more robust to real time engine running conditions.

Table 3.1. Engine configuration.

ENGINE	SPECIFICATION
Model	Cummins ISB 6.7L
Configuration	Inline 6 cylinder
Rated Power	325 hp
Peak Torque	650 lb-ft @ 1500 RPM
Aspiration	Variable Geometry Turbocharger (VGT)

The GE Dynamometer provides demanded speed and torque load to the engine. A MIMO (Multi-input Multi-output) dSPACE controller was programmed by Ryan Schultz to set up torque and speed control. Table 3.2 shows detailed information regarding the dynamometer.

Table 3.2. Dynamometer configuration.

DYNO	SPECIFICATION
Model	GE - 1G473
Excitation volts	60 Volts
Maximum Power	800 hp
Controller	DyneSystem Dyn-Loc IV

The complete experimental setup is shown in Figure 3.1 and Figure 3.2. The ISB engine is connected with the dyno; the exhaust air goes through the exhaust pipe and flows downstream to go through instrumented DOC. During normal running conditions, the EGR valve is opened, and emission analyzers are installed upstream and downstream (not presented in the picture).

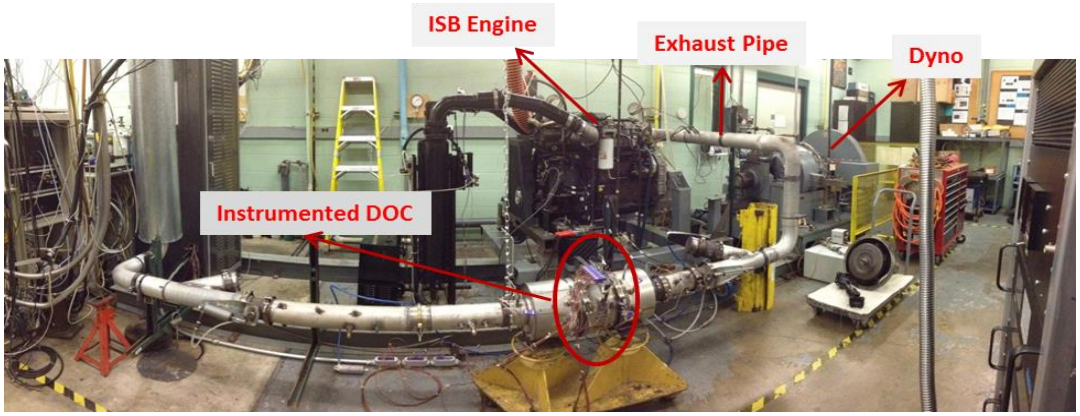

Figure 3.1. Picture of the overall setup in the engine laboratory.

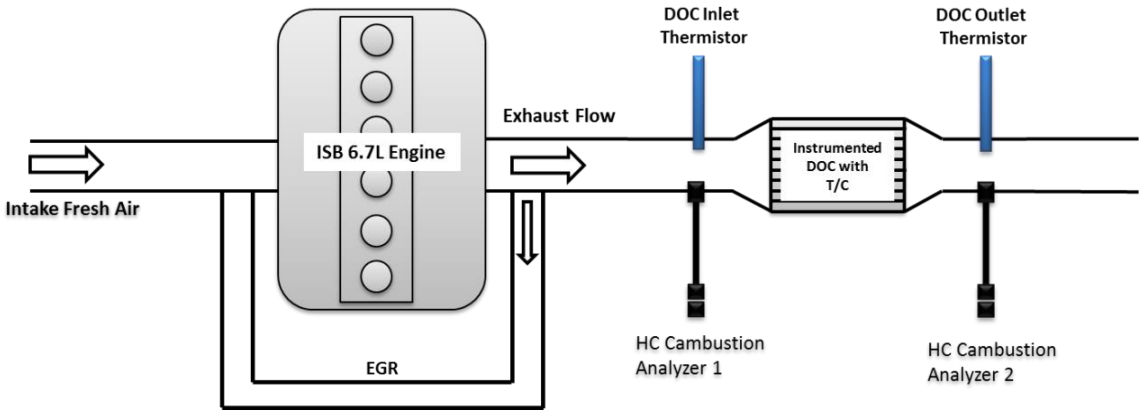

Figure 3.2. Picture of the overall setup in the engine laboratory.

As the aim of the thesis project is to model the DOC, the DOC used in the experiment is provided by Cummins. The property of the DOC is listed in Table 3.3. Since only physical parameters of the DOC are provided, some parameters for modeling require approximation based on publications.

Table 3.3. DOC properties list table.

Parameters:	DOC
Diameter (in)	9.75 inch
Length (in)	4 inch
Configuration	Flow through
Substrate Material	Cordierite
Cell Density	400 cpsi
Catalyst Material	Pt/Pd

Figure 3.3 is a picture of the installed DOC. Twelve thermocouples are located in three axial locations and 4 radial locations. Detailed locations of thermocouples are presented in Figure 3.4.

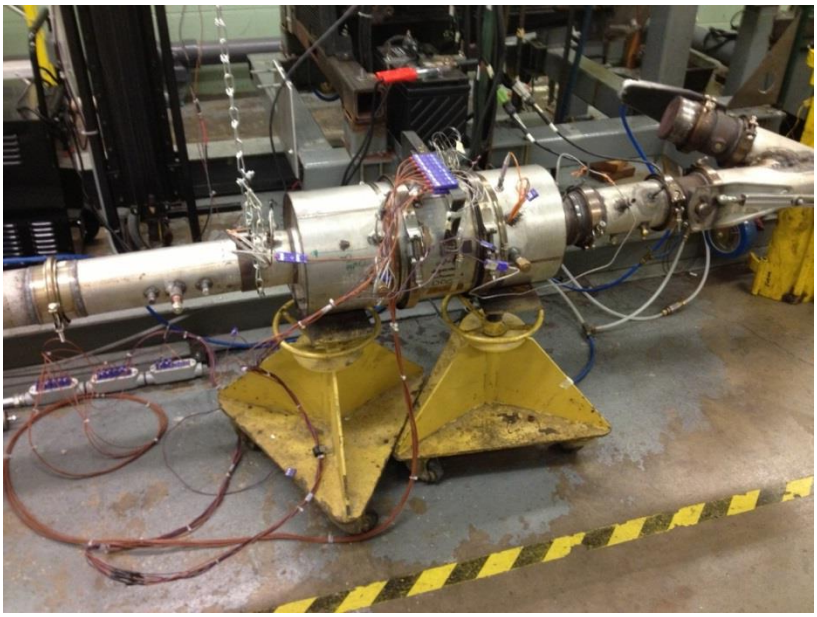

Figure 3.3. Aftertreatment Setup with only DOC in place.

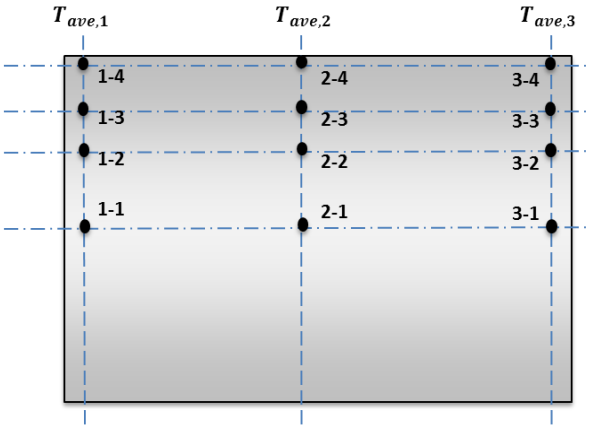

Figure 3.4. DOC Thermocouple instrumentation diagram.

3.2 Hybrid Model Description

This section describes the hybrid model in calibrating DOC-out NO and NO_2 concentrations. Reactions and theories are discussed in detail. First, the reaction is listed below:

$$NO + \frac{1}{2} O_2 \xleftrightarrow{DOC\ catalyst} NO_2, \tag{3.1}$$

NO oxidation reaction is a reversible, exothermic reaction as shown below:

$$r_{NO} = k_{NO} \left(C_{NO} {C_{O_2}}^{0.5} - \frac{C_{NO_2}}{K_{NO}} \right), \tag{3.2}$$

the overall reaction rate is the rate of forward reaction minus reverse reaction. There are two important facts here. First, k_{NO} is Arrhenius reaction rate constant given by the following equation:

$$k_{NO} = A_{NO} e^{-(\frac{Ei}{RT})}, \tag{3.3}$$

while A_{NO} is the pre-exponential for the reaction, and *Ei* is the activation energy, *T* is the reactor temperature, *R* is the universal gas constant, when unit is in international unit formatting, *R* is 8.314. From equation 3.3 it can be seen that reaction rate constant is a function of reactor temperature. Thus, kinetically speaking, the higher the temperature is, the faster the reaction rate is. If reaction is irreversible, then the reaction rate is simply determined by kinetics, which will result in more reactant being converting into product. However, this might not be the case in a reversible reaction. Reversible reaction is determined by two components, first is kinetics, which we just discussed, and the second is thermodynamics.

NO oxidation thermodynamics is determined by K_{NO} , which is the thermodynamic equilibrium constant:

$$K_{NO} = \frac{RTe^{-(\frac{\Delta G}{RT})}}{P}, \tag{3.4}$$

and equation

$$\Delta G = \Delta H + T\Delta S = -58190 + 73.236T \tag{3.5}$$

describes the detailed method for calculating K_{NO}. K_{NO} determines where the final dynamic equilibrium lies, as shown in Figure 3.5. From Equation 3.4, it can be found that the higher the temperature is, smaller K_{NO} is, which means higher temperature favors the reverse reaction-- NO_2 reduction.

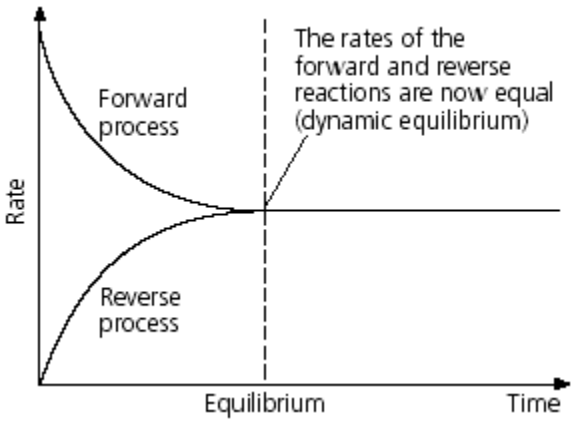

Figure 3.5. Reversable reaction dynamic equilibrium [36].

After the discussion of chemical reaction basics in DOC, it can be concluded that A method of simplification is to define $K_p = \frac{C_{NO_2,outlet\ DOC}}{C_{NO,outlet\ DOC}C_{O_2,outlet\ DOC}^{0.5}}$ in all cases regardless of whether the reaction reaches equilibrium at the DOC outlet. Kp is low in comparatively very low temperature because of kinetic limitation and in very high temperature because thermodynamic equilibrium favors the reverse reaction. It can be predicted that there occurs a 'peak' in DOC downstream Kp as a function of DOC temperature.

K_p here only makes sense when the reaction reaches equilibrium. The green dash line in Figure 3.6 demonstrates the Equilibrium K_p as a function of temperature, which matches with the experimental conversion only under high temperature condition.

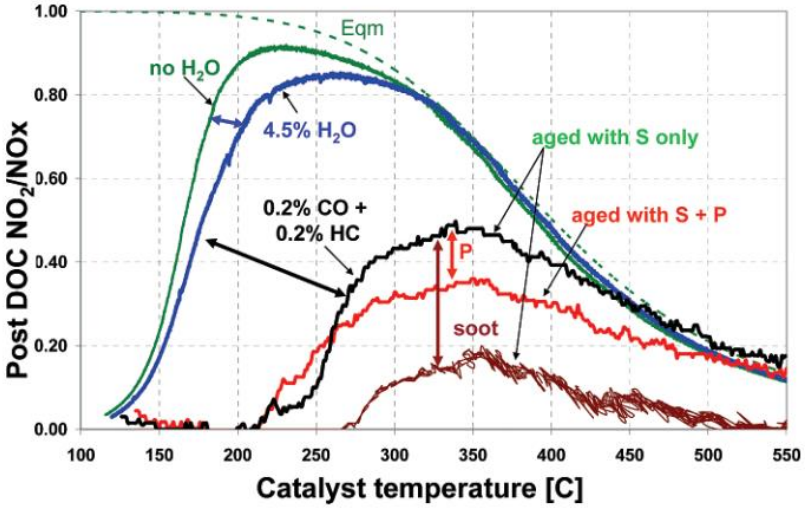

Figure 3.6. NO_2/NO_x as a function of temperature [37].

The reason behind this is because during comparatively low temperature (lower than 350 C), the reaction rate is lower such that the lower the temperature is, the further away the reaction is from equilibrium. Furthermore, A_{NO} and Ei term vary with setpoint (different rpm, torque), which brings difficulty in calibration of pre-exponential factor and activation energy as it brings too many degrees of freedom.

The method to define $K_p = \frac{C_{NO_2,outlet\ DOC}}{C_{NO,outlet\ DOC} C_{O_2,outlet\ DOC}^{0.5}}$ has the advantage as follows. First, K_p will be a function of only temperature, regardless of different setpoint of engine. Second, the phenomenon of reaction rates getting smaller as the DOC ages will be represented by a decrease in K_p.

As NOx and NO analyzers are only able to measure concentration in ppm, to get mol/m3 unit of concentration, it requires the temperature and pressure information.

Pressure is assumed as 101.3 KPa as one atmosphere. However, there are 12 thermocouples installed in DOC, and here in this model thermocouple 2-1 is used because this thermocouple lies exactly in the middle of the DOC, which is a good indicator of the DOC temperature. There is very slight variation between thermocouples, the temperature range between 3-1 position and 1-1 position are within 5 Celsius.

Figure 3.7 shows the schematic of this hybrid model, which takes input of DOC temperature, DOC out NOx, and DOC out Oxygen concentration, and predicts downstream DOC NO and NO_2 concentration. The input of oxygen is indicated in a different color because we currently don't have Oxygen sensor installed, however the detailed indirect calculation of oxygen concentration is discussed in section 4.5. Also, since there is no direct NO_2 analyzer, NOx is subtracted by NO to get the indirect NO_2 measurement.

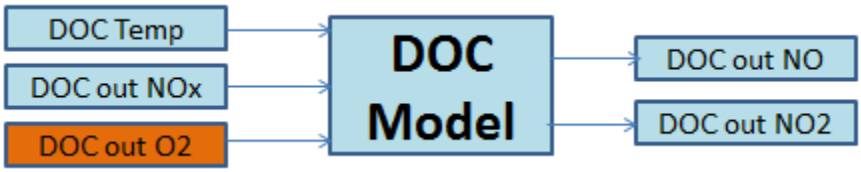

Figure 3.7 Schematic of the hybrid DOC model

After modeling *Kp* as a function of temperature, the next task is to apply *Kp* to experimental NO_x data. With input of Kp, C_{O_2} and C_{NOx}, concentrations of NO and NO_2 can be calculated using the following formulas:

$$C_{NO_2} = \frac{\sqrt{C_{O_2}} \times K_P}{\sqrt{C_{O_2}} \times K_P + 1} \times C_{NOx}, \tag{3.7}$$

$$C_{NO} = \frac{1}{\sqrt{C_{O_2}} \times K_P + 1} \times C_{NOx}\ . \tag{3.8}$$

Equation 3.7.and 3.8. are rearranged from $K_p = \frac{C_{NO_2,outlet\ DOC}}{C_{NO,outlet\ DOC} C_{O_{2,outlet\ DOC}}^{0.5}}$, while NOx is considered only NO and NO_2.

3.3 First-degree-aged DOC Experimental Data and Calibration

The experiment stared with first-degree-aged DOC rather than fresh DOC because prior to the experiment, the DOC has been under research of HC light-off temperature modeling under different thermal aging levels that DOC has already been through a cycle of thermal aging.

Experiments have been conducted at 5 different speeds and 4 different torques. Selected speeds were 1200 rpm, 1350 rpm, 1500 rpm, 1650 rpm and 1800 rpm. Selected torques being 100 lb-ft, 200 lb-ft, 300 lb-ft, 350 lb-ft. DOC out NO and NO_x concentrations as well as DOC temperatures were captured to calibrate the K_p term. Table 3.4 shows the experimental points selected to calibrate the K_p curve. K_p calibration results are presented in Figure 3.7.

Table 3.4. First-degree-aged DOC out measurement.

Setpoint	DOC out NO (ppm)	DOC out NO_x (ppm)	DOC temp (K)	Kp calculated
1200 rpm, 100 lb-ft	377.9679392	403.0617215	442.3058802	0.028659
1200 rpm, 200 lb-ft	446.6166986	677.1599095	521.4343662	0.244167
1200 rpm, 300 lb-ft	406.3057485	844.3112744	604.672512	0.551642
1200 rpm, 350 lb-ft	471.6758831	914.1176647	642.903933	0.494663
1350 rpm, 100 lb-ft	370.9920058	453.1869812	439.9253295	0.044337
1350 rpm, 200 lb-ft	525.4912178	616.5488649	543.2687275	0.350878
1350 rpm, 300 lb-ft	651.7339045	737.3488049	635.7176977	0.519366
1350 rpm, 350 lb-ft	752.6582358	849.7889484	668.9572504	0.422033
1800 rpm, 100 lb-ft	278.5212126	317.879229	476.5046087	0.064111
1800 rpm, 200 lb-ft	164.9451623	306.8262456	577.3027144	0.429544

Table 3.4. Continued.

1800 rpm, 300 lb-ft	310.4967245	361.834455	744.2351162	0.093747
1800 rpm, 350 lb-ft	347.7269991	369.6170516	800.9734234	0.037029

It can be seen witnessed in Figure 3.7 that K_p can be modeled as a Gaussian distribution, such that K_p can be easily captured with only one input- DOC temperature regardless of different engine speed and torque conditions, as shown in equation 3.6

$$K_P = y_0 + \frac{A}{w \times \sqrt{\frac{\pi}{2}}} \times e^{\left(\frac{-2 \times (T_{DOC} - x_c)}{w}\right)^2}. \quad (3.6)$$

The reason for choosing Gaussian form of Kp is because different nonlinear fitting curve has been applied, including polynomial distribution, Weibull distribution fitting. It was found that Gaussian distribution curve is able to provide the best fitting s compared to the experimental data. Nonlinear fitting is conducted through software named OriginPro 8. In OriginPro 8, Newton's method is embedded in parameter optimization.

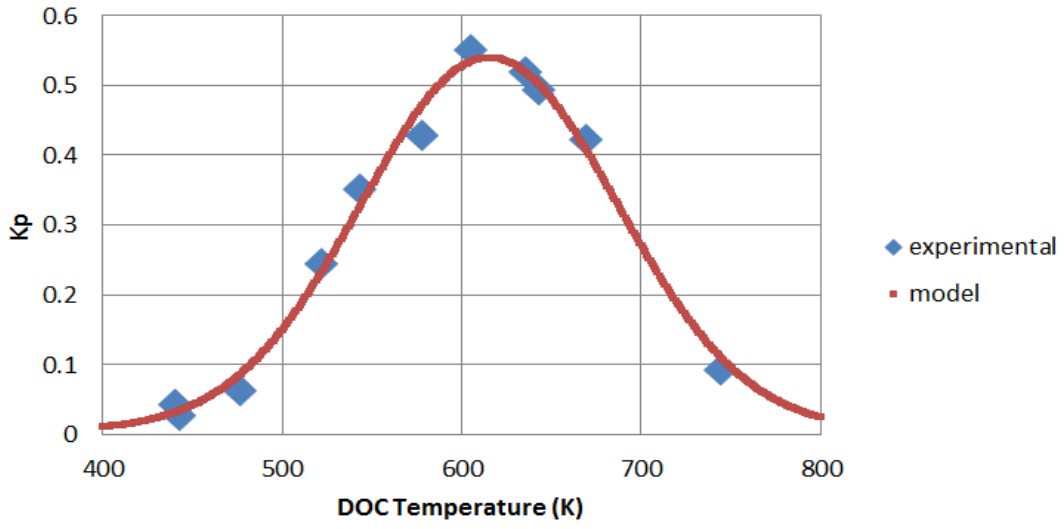

Figure 3.8. Kp as a function of DOC temperature for first-degree-aged case.

The calibrated parameters for the Gaussian distribution are listed in Table 3.5. At this point, the first-degree-aged DOC has been calibrated and first-degree-aged DOC *Kp* will be only a function of DOC temperature.

Table 3.5. Calibrated parameter for first-degree-aged DOC.

	Parameter value
y_0	0.005998593
x_c	615.3603029
w	142.8901865
A	95.65060446

3.4 DOC Aging Procedure

The aging procedure was carried out at Alcoa in Lafayette, IN, and the detailed aging procedure is listed in Table 3.4. It has been proved that 650 °C for 20 hours can be long enough to result in the decrease of PMG (particular metal group) effective sites, such that the oxidation of NO will be less effective.

Table 3.6. Aging procedure of DOC.

Temperature °C	Durations (hours)	Descriptions
25-650	2	Initial warm-up
650	20	Main aging
650-25	15	Oven cool-down

3.5 Aged DOC Experiment and Calibration

After the aging procedure, the DOC was reinstalled to the engine bench and previous setpoints were duplicated. 18 steady state setpoints were applied as input in calibrating the K_p term. In real experiments, 20 setpoints were included in the entire

experimental procedure, with speeds at 1200 rpm, 1350 rpm, 1500 rpm, 1650 rpm, 1800 rpm, and the torques at 100 lb-ft, 200lb-ft, 300lb-ft, 350lb-ft. However, some setpoints have poor steady-state behavior, which were not included in the calibration. Those outstanding experimental conditions are discussed in section 4.3.

Table 3.7. Second-degree-aged DOC out measurement.

set point	DOC out NO (ppm)	DOC out NO_x (ppm)	DOC temp (K)	Kp calculated
1200 rpm, 100 lb-ft	449.7976238	479.5737302	436.0606136	0.028611
1200 rpm, 200 lb-ft	441.1053517	747.6487004	533.6466934	0.343298
1200 rpm, 300 lb-ft	493.4523791	929.7280908	621.230138	0.46224
1200 rpm, 350 lb-ft	591.8474422	1035.767645	666.0404009	0.402324
1350 rpm, 100 lb-ft	433.6186843	471.2867511	434.8799423	0.037654
1350 rpm, 200 lb-ft	338.1676083	596.0524325	543.2689306	0.396609
1350 rpm, 300 lb-ft	422.8150753	786.2147	638.6316472	0.456694
1350 rpm, 350 lb-ft	542.4383865	913.9206	681.8841664	0.380273
1500 rpm, 100 lb-ft	391.1031674	417.1279731	448.0492808	0.02928
1500 rpm, 200 lb-ft	207.1549399	381.7218092	574.6375081	0.435306
1500 rpm, 300 lb-ft	164.3319104	178.8725757	751.3381767	0.048613
1650 rpm, 100 lb-ft	313.8431356	334.372638	444.4407996	0.016937
1650 rpm, 200 lb-ft	177.5606155	315.9794457	583.6858628	0.394074
1650 rpm, 300 lb-ft	298.0012962	361.5878372	723.2450992	0.158087
1800 rpm, 100 lb-ft	209.3518795	238.212	457.0988824	0.061973
1800 rpm, 200 lb-ft	156.3689002	271.653	617.408655	0.370718
1800 rpm, 300 lb-ft	284.4626979	313.3864912	762.6066186	0.062054
1800 rpm, 350 lb-ft	318.4473591	334.0431089	819.8819559	0.030699

Figure 3.8 shows K_p as a function of DOC temperature and the model Kp curve, which is only a function of temperature. The red model K_p will be applied in Chapter 4 for modeling applications. Detailed calibrated constants are listed in Table 3.8 for further reference.

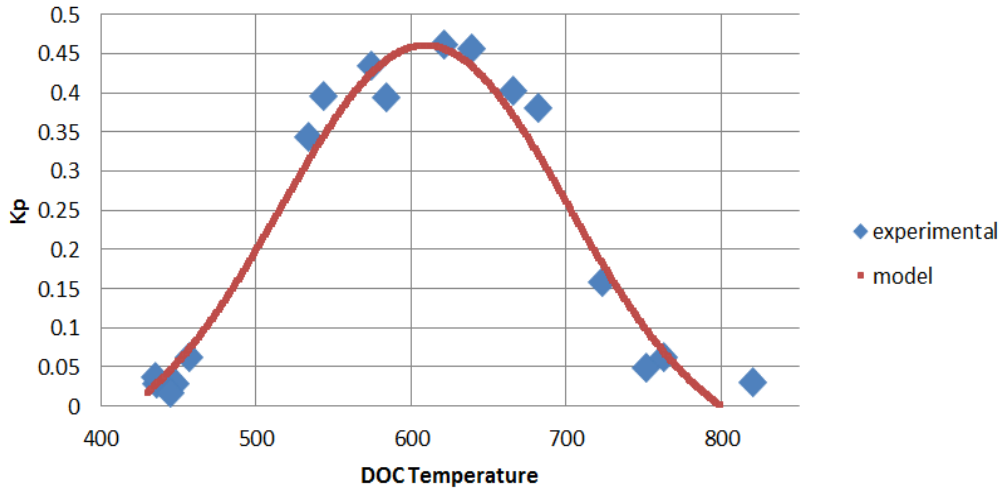

Figure 3.9. Kp as a function of DOC temperature for Second-degree-aged case.

Table 3.8. Calibrated parameter for second-degree-aged DOC

	Parameter value
y_0	-0.062662812
x_c	609.1608959
w	185.1155098
A	121.4003608

From Figure 3.9, it can be seen that second-degree-aged K_p is lower than first-degree-aged DOC K_p in Figure 3.7, which means that at the same temperature in the DOC, less NO is converted into NO_2, as a matter of aging, which is considered normal behavior of catalyst aging.

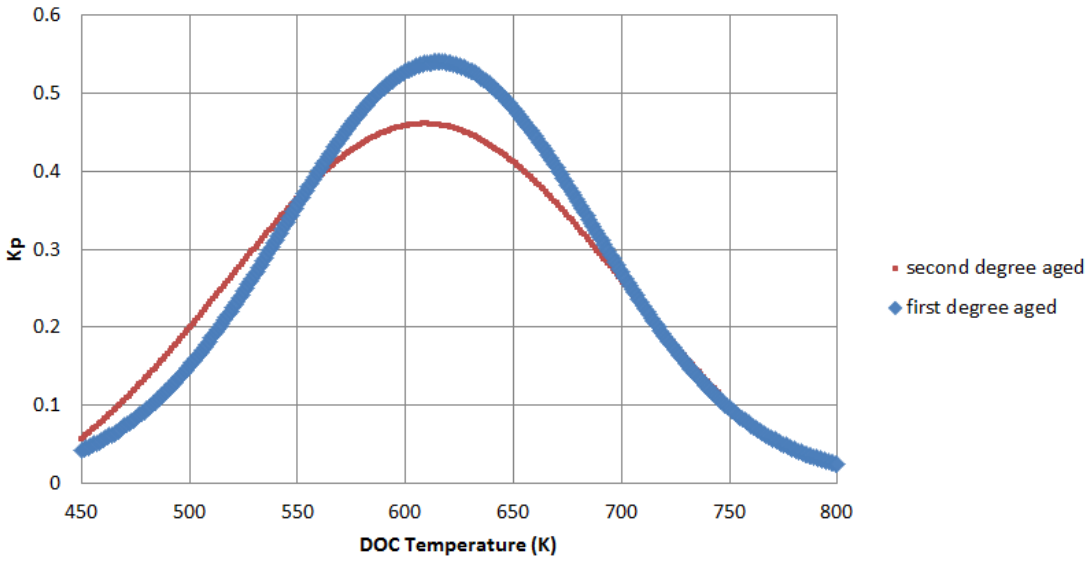

Figure 3.10. Kp shift featuring both freshness level of DOC.

3.6 Light-off Temperature Shift

From the previous experimental data, the K_p curve has been calibrated for the current freshness level. To define the current freshness level of DOC, hydrocarbon light-off temperature is calculated using the equation below:

$$\text{Conversion of HC\%} = \frac{[\text{HC}]\text{upstream} - [\text{HC}]\text{downstream}}{[\text{HC}]\text{upstream}}\%. \tag{3.9}$$

Two sets of experiments were carried out both for fresh DOC and aged DOC. The light-off temperature for hydrocarbon has been significantly increased, as shown in. Also, the repeatability of two sets of test proved the experiment to be reliable. First, two sets of first-degree-aged DOC HC light-off temperatures at 1350 rpm were measured and calculated: they are 430.652 K and 437.219 K. There is a minor difference in these two sets of experimental results, which is considered acceptable. Also, two sets of second-degree-aged DOC HC light-off temperatures at 1350 rpm were measured and calculated:

they are 503.851 K and 498.477 K. The difference between two sets of experimental results is also within 10% error.

Table 3.9. Light-off temperature shift measurement.

	First-degree-aged DOC	Second-degree-aged DOC
HC light-off @ 1350 rpm (K)	430.652	503.851
HC light-off @ 1350 rpm (K)	437.219	498.477

To better illustrate the light-off temperature calculation, HC conversion rate and torque, the DOC temperature has been plotted separately as a function of time. It can be seen in Figure 3.10 through Figure 3.12 that the first-degree-aged DOC, light-off occurs when the torque is at 100 lb-ft. As the temperature goes higher, the conversion of hydrocarbon gradually reaches 100%.

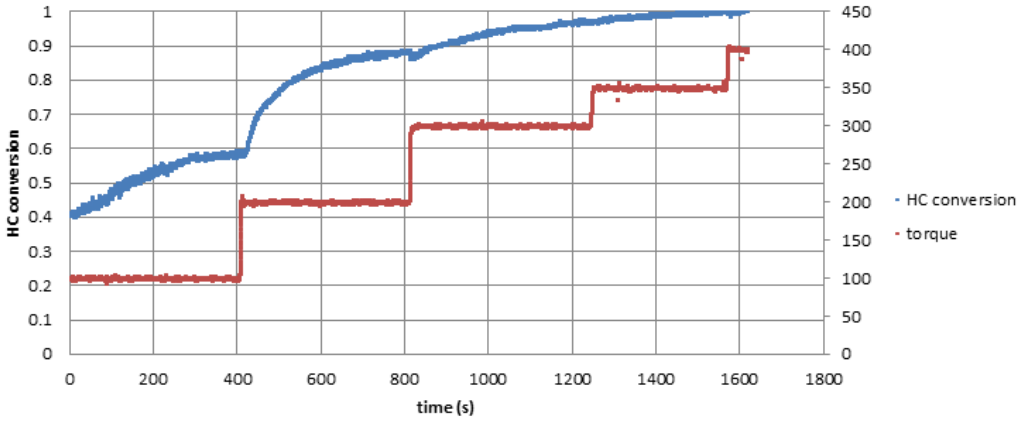

Figure 3.11. HC conversion and torque as a function of time @1350 rpm.

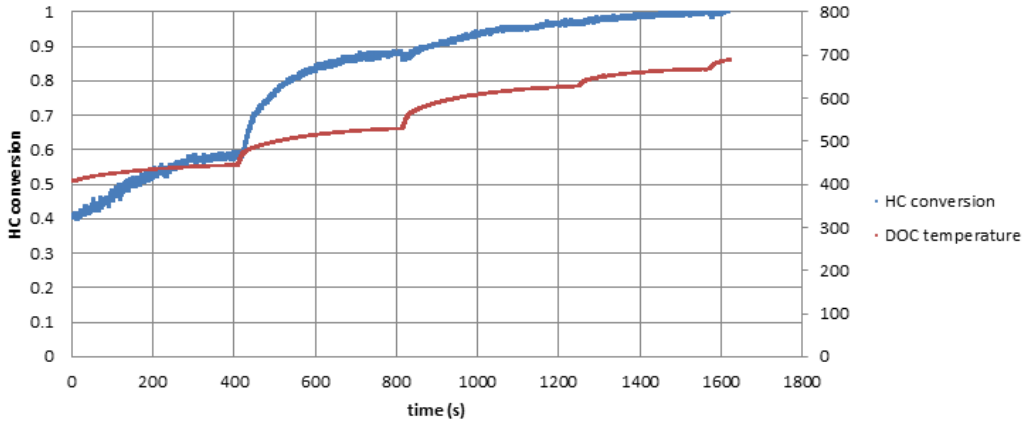

Figure 3.12. HC conversion and DOC temperature as a function of time @1350 rpm.

From Figure 3.10, it can be seen that at 1350 rpm set point, the engine maintains constant engine torque 100, 200, 300 and 350 lb-ft. The HC conversion rate goes up along with the time, as torque goes up. From Figure 3.11, it is shown that HC conversion goes up as the temperature of the DOC increases. The trend of HC conversion rate is very similar to the increase of DOC temperature. Due to this fact, DOC temperature can be used as an input in modeling HC conversion rate. Thus, Figure 3.12 shows the figure of HC conversion vs DOC temperature when DOC is first-degree-aged. This plot provides useful information in finding out the corresponding DOC temperature when HC conversion rate reaches 50%, in this case at 430.652 K. This temperature is called the first-degree-aged DOC HC light-off temperature during 1350 rpm engine condition.

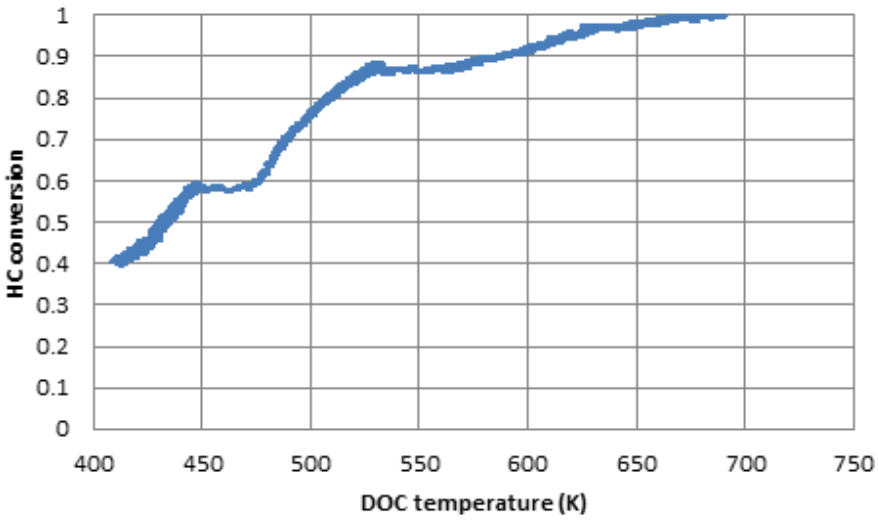

Figure 3.13. HC conversion as a function of DOC temperature @1350 rpm.

Figure 3.13 through Figure 3.15 show three different plots for the second-degree-aged DOC. Similarly, hydrocarbon conversion rate is plotted along with torque and DOC temperature. However, this time 100 lb-ft is not able to bring high enough temperature to achieve light-off. Hydrocarbon light-off occurs during 200 lb-ft, and there is a considerably larger temperature increase as compared to the first-degree-aged DOC case.

In Figure 3.13 there is a notch of HC conversion corresponding to 100s to 200s in time axis, which means during this range, the HC conversion has decreased. This might be caused by the sudden change of the engine torque as we can see the decrease happens right after engine torque increased to 200 lb-ft. Further investigation will be required to analyze the reason for the decrease of conversion rate.

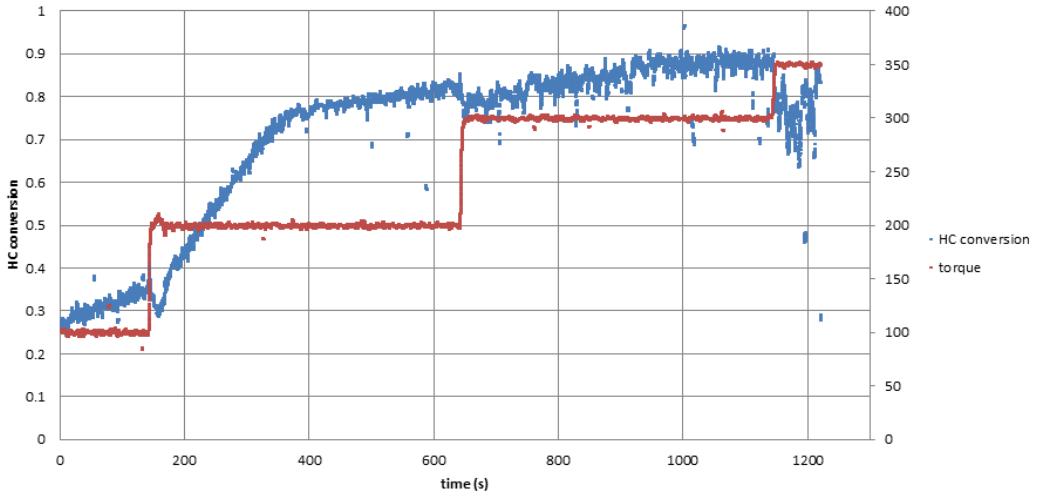

Figure 3.14. HC conversion and torque as a function of time @1350 rpm.

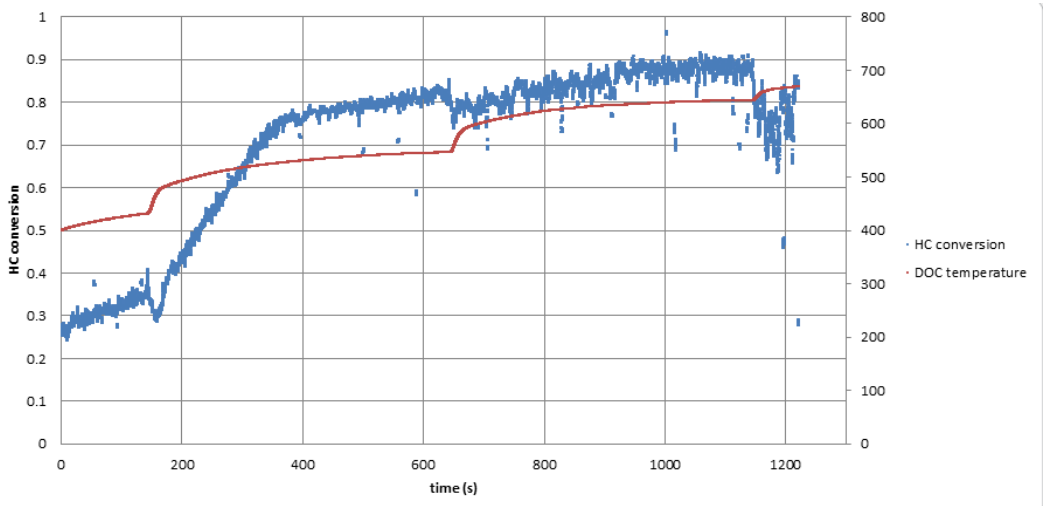

Figure 3.15. HC conversion and DOC temperature as a function of time @1350 rpm.

Figure 3.15 shows HC conversion vs DOC temperature when DOC is second-degree-aged. This plot provides useful information in finding out the corresponding DOC temperature when HC conversion rate reaches 50%, in this case here is 503.851K. This temperature is called the second-degree-aged DOC HC light-off temperature during 1350 rpm engine condition.

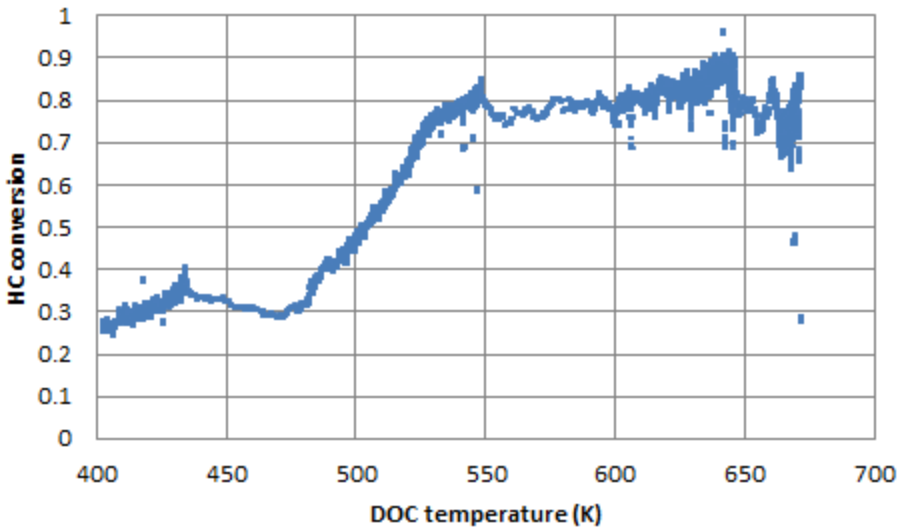

Figure 3.16. HC conversion as a function of DOC temperature @1350 rpm.

3.7 Preliminary Modeling of NO/NO_2 Ratio as A Function of Light-off Temperature

Section 3.3 and section 3.5 discussed first-degree-aged and second-degree-aged DOC *Kp* calibration. Section 3.6 described the HC light-off temperature shift from first-degree-aged DOC to second-degree-aged DOC. Sutjiono [6] developed a model that could predict the HC light-off temperature as a function of temperature inside the DOC using thermal balance. The model Sutjiono developed is able to capture the correlation between catalyst aging and light-off temperature shift. Thus, if NO/NO_2 ratio can be modelled as a function of HC light-off temperature, then finally NO/NO_2 ratio at different DOC aging levels can be predicted with input of only DOC temperature.

To make sure the assumption of the model is plausible, it needs to be proved that the DOC has comparatively small selectivity in oxidation, which means DOC aging has the same amount of impact on NO oxidation and HC oxidation. This phenomenon is difficult to quantitatively observe. However, previous researchers have conducted experiments that support this assumption.

Usmen [40] conducted research on fresh and aged three-way catalyst NO, HC and CO light-off temperature, comparing the light-off temperature shift, and indicated that light-off temperature for HC is increased by 31 K, CO increased 39 K, and NO increased 38 K. The catalytic metal in the experimented three-way catalyst is Pt, same with the catalyst in our experiment. Winkler [41] experimented on diesel oxidation catalyst and the results of different aging levels on conversion performance of DOC are shown in Figure 3.16. Conversion plots for CO, NO and HC for DOC new, DOC first-degree aged. It can be seen that the DOC aging level has almost the same effectiveness impact on all three species. Thus, it can be concluded that HC light-off temperature shift might be able to indicate NO_x oxidation shift relatively well.

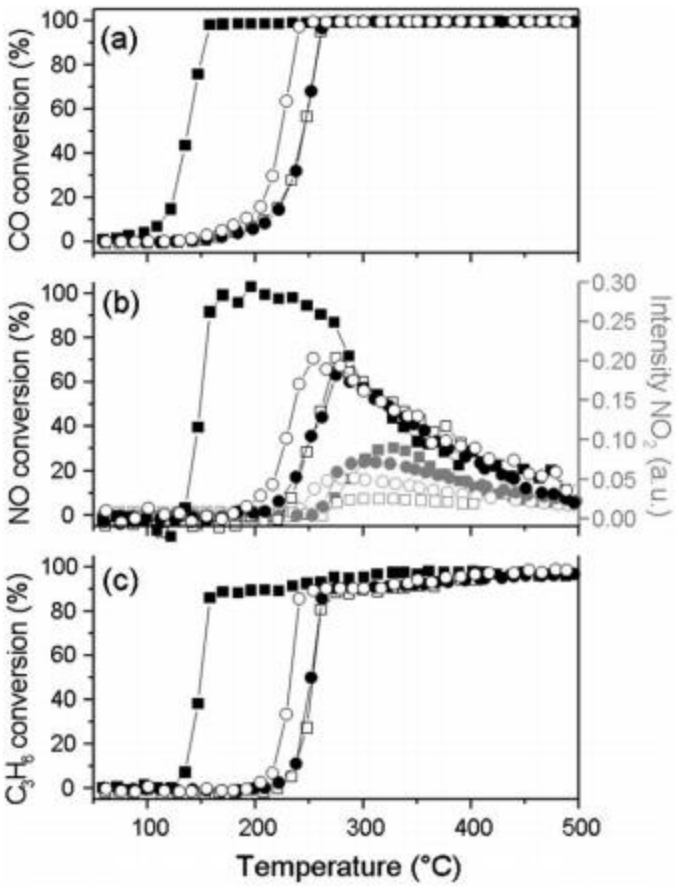

Figure 3.17. Conversion plots for CO, NO and HC for DOC new, DOC first-degree aged, second-degree-aged DOC [40].

Now that we have clarified that DOC aging has the same impact in reducing the effectiveness level of the catalyst in oxidizing HC and NO, the next task is to build light-off temperature into the model. Lassi [24] conducted research on how thermal aging temperature and aging time affect the effective surface area for the catalyst. TPD (Temperature programmed desorption) is conducted to compare the aged catalyst effective surface with the fresh catalyst effective surface. Figure 3.17. Effect of aging temperature on the active surface area shows how different aging temperature and time result in loss of active surface area. It can be seen that, for lower temperatures, the effect

that aging has on reduction of surface sites is almost linear. The aging procedure in our case is 650 C for 20 hours, and we consider that the aging time in such condition is reducing the effective surface area linearly as a function of time. Thus, it is assumed that the reaction rate in aged catalyst is also reduced linearly as a function of aging time.

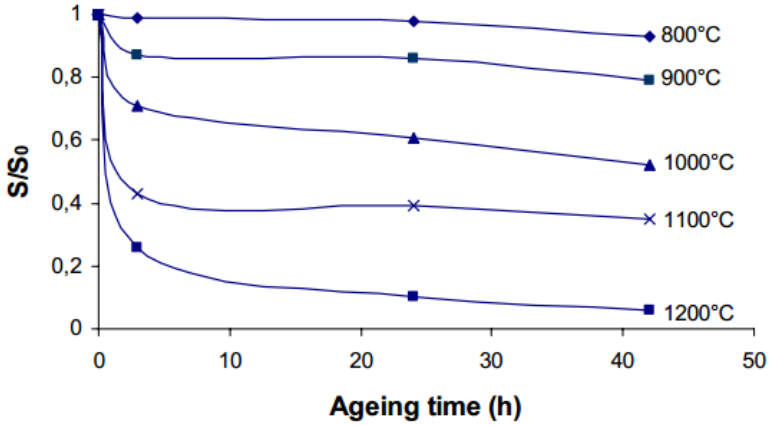

Figure 3.18. Effect of aging temperature on the active surface area [24].

With the assumption discussed above, a preliminary Kp model is built as a function of HC light-off temperature named *T* in Table 3.10. The complete Kp curve requires the input of DOC light-off temperature. When both light-off temperature inputs are available, the 3-D model of Kp as a function of HC light-off temperature and DOC temperature is shown in Figure 3.18.

Table 3.10. linear interpolation parameters for Kp as a function of HC light-off temperature.

	First-degree -aged DOC	Second-degree -aged DOC	Linear fitting parameter by HC light-off temperature shift
y0	0.005998593	-0.062662812	0.005998593 - 0.000967062*(T-432)
xc	615.3603029	609.1608959	615.3603029 - 0.087315591*(T-432)
w	142.8901865	185.1155098	142.8901865 + 0.594722863*(T-432)
A/w	0.669399396	0.655808694	0.669399396 - 0.000191418*(T-432)

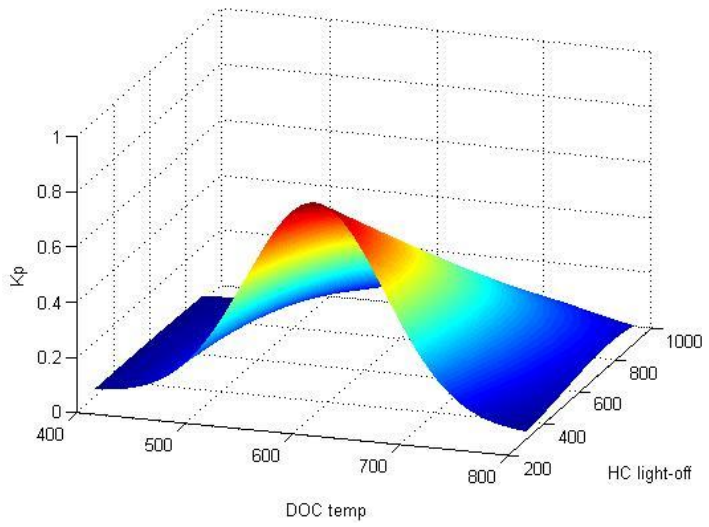

Figure 3.19. 3-D model of Kp as a function of HC light-off temperature and DOC temperature.

Since only first-degree-aged DOC and second-degree-aged DOC experimental data are involved in this calibration, the *Kp* model as a function of light-off temperature is preliminary and will require further aging stages to prove the overall reliability of the model.

CHAPTER 4. RESULTS AND DISCUSSION

In this chapter, first-degree-aged DOC-out experimental and modeling NO and NO_2 concentrations are compared and analyzed in section 4.1. Second-degree-aged DOC out experimental and modeling NO and NO_2 concentrations are compared and analyzed in section 4.2. Fluctuations in some abnormal setpoints are discussed in detail in section 4.3 to further analyze the robustness of the model. The averaging involved in processing the data is presented in section 4.4.

4.1 First-degree-aged DOC Experimental and Modeling Results

Table 4.1. Percentage of model points outside 10% allowance of real data.

	speed	NO	NO_2
First-degree-aged DOC	1200 rpm	0.73%	0.73%
	1350 rpm	0.00%	0.00%
	1500 rpm	2.62%	4.52%
	1650 rpm	0.28%	0.28%
	1800 rpm	2.28%	2.28%

Table 4.1 shows the percentage error of the model from the real experimental data. To calculate modeled NO and NO_2 concentration, NO_x is required as another input apart from DOC temperature. Since K_p determines the ratio of NO/NO_x, with the input of NO_x, NO and NO_2 concentrations can be easily calculated.

To reemphasize the modeling criteria, since there is no oxygen sensor available in setup, oxygen concentration is kept constant at 19% by volume. NO_2 is calculated by subtracting NO from NOx measurement.

In this section, Figure 4.1, Figure 4.5, Figure 4.9, Figure 4.13 and Figure 4.17 show first-degree-aged DOC NO model vs real concentration at 1200, 1350, 1500, 1650 and 1800 rpm. Dashed lines are 10% error above and below y=x. Any data points outside the dashed lines are considered abnormal points, and the percentage of the abnormal points is statistically calculated and listed in Table 4.1. The largest NO model vs real concentration error occurred at 1500 rpm, which is 2.62%. This means that 2.62% modeled data points are not within 10% error of the experiment. Most of the modelled data points can reflect precisely where the real experimental points lie.

Figure 4.2, Figure 4.6, Figure 4.10, Figure 4.14 and Figure 4.18 show first-degree-aged DOC NO_2 model vs real concentration at 1200, 1350, 1500, 1650 and 1800 rpm. The trend of NO_2 model vs real concentration is very similar to NO model vs real concentration. However, since usually the concentration of NO_2 is smaller than that of NO, the range of concentrations of NO_2 is smaller. The largest NO_2 model vs real concentration error occurred at 1500 rpm, which is 4.52%. This means that 4.52% modeled data points are not within 10% error of the experiment. Most of the modelled data points can reflect precisely where the real experimental points lie. The reason for the comparatively larger error at 1500 rpm might be the issue with the unstable charge flow. The issue of flow fluctuation at 1500 rpm will be further discussed in section 4.3.

Figure 4.3, Figure 4.7, Figure 4.11, Figure 4.15 and Figure 4.19 show first-degree-aged DOC NO real and model concentrations vs time at 1200, 1350, 1500 1650

and 1800 rpm. These figures are able to present clearly how DOC-out NO concentrations change with time. Modelled-DOC out NO concentrations are plotted on the same figures to give a better intuition about how good the matching is between the experimental data and the model.

Figure 4.4, Figure 4.8, Figure 4.12, Figure 4.16 and Figure 4.20 show first-degree-aged DOC NO_2 real and model concentrations vs time at 1200, 1350, 1500, 1650 and 1800 rpm. In the real experiment, since analyzers only measure NO and NO_x concentrations, there is no direct way of measuring experimental NO_2. NO_x minus NO concentration is calculated as experimental DOC-out NO_2 concentration. During experimental measurement, it was seen that there is excessive noise in NO_x measurement so that averaging and data processing had to be applied. The detailed NO_x concentration averaging will be discussed further in section 4.4.

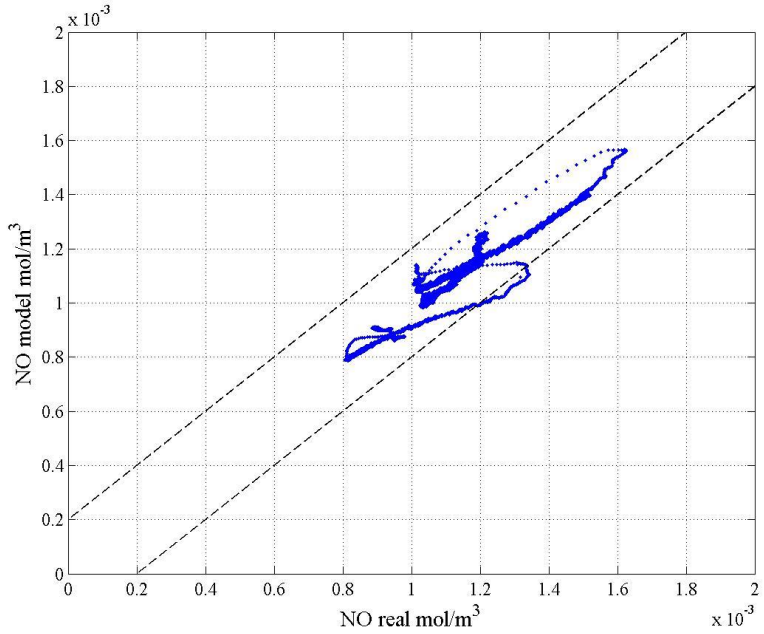

Figure 4.1. First-degree-aged DOC @1200 rpm NO model vs real.

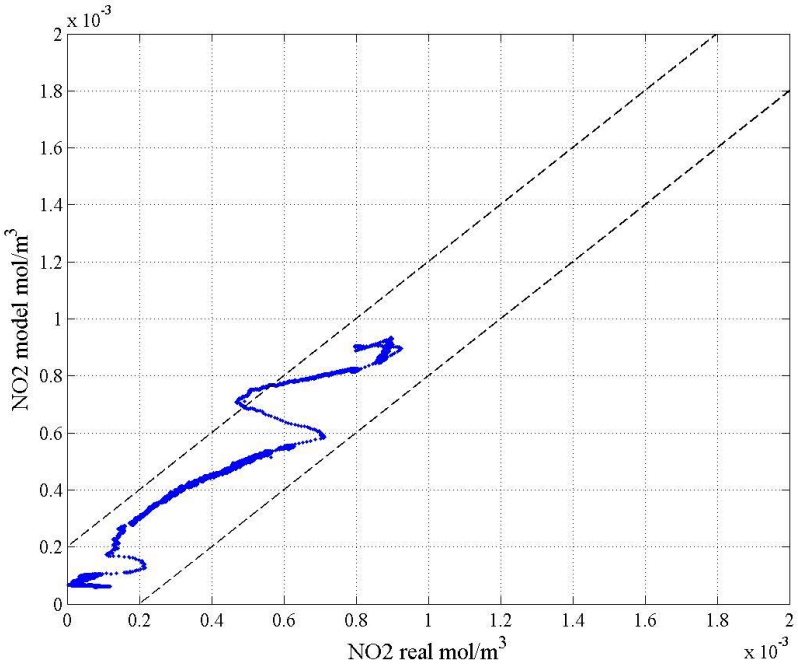

Figure 4.2. First-degree-aged DOC @1200 rpm NO_2 model vs real.

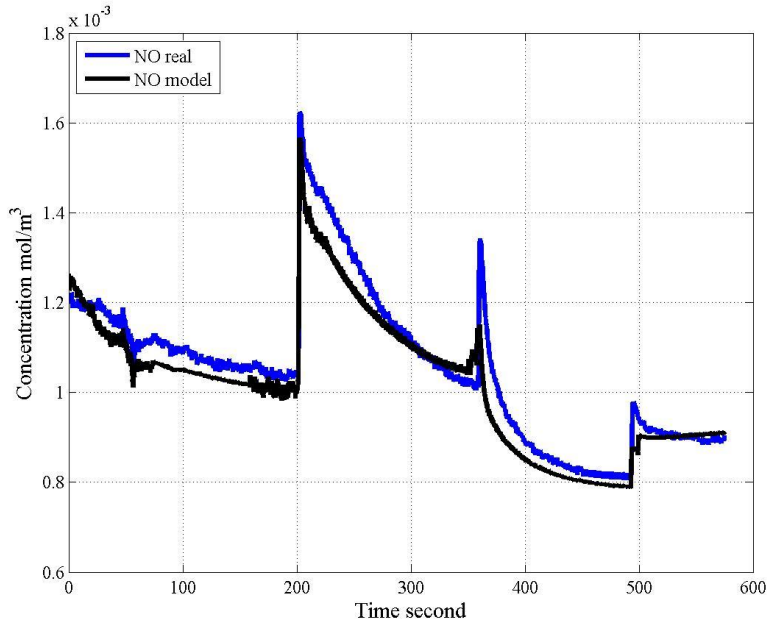

Figure 4.3. First-degree-aged DOC @1200 rpm NO real, NO model vs time.

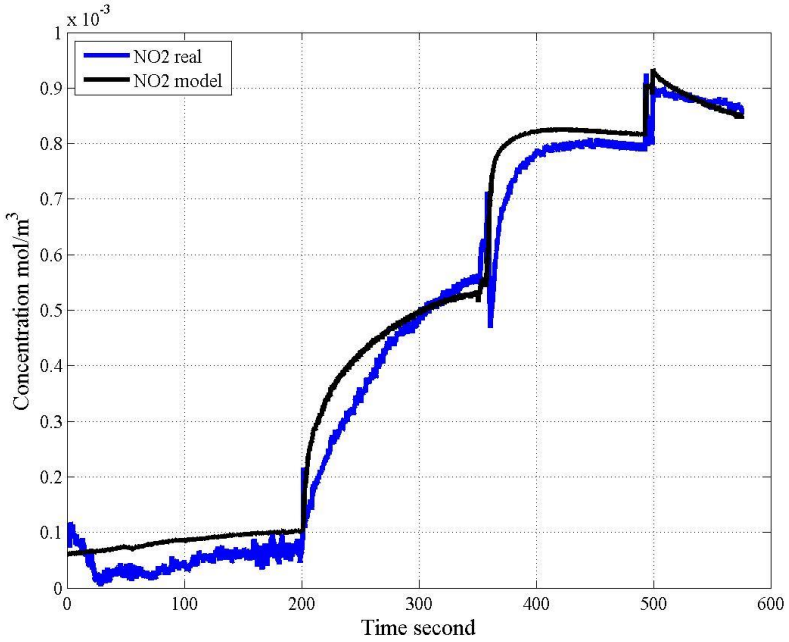

Figure 4.4. First-degree-aged DOC @1200 rpm NO_2 real, and model vs time.

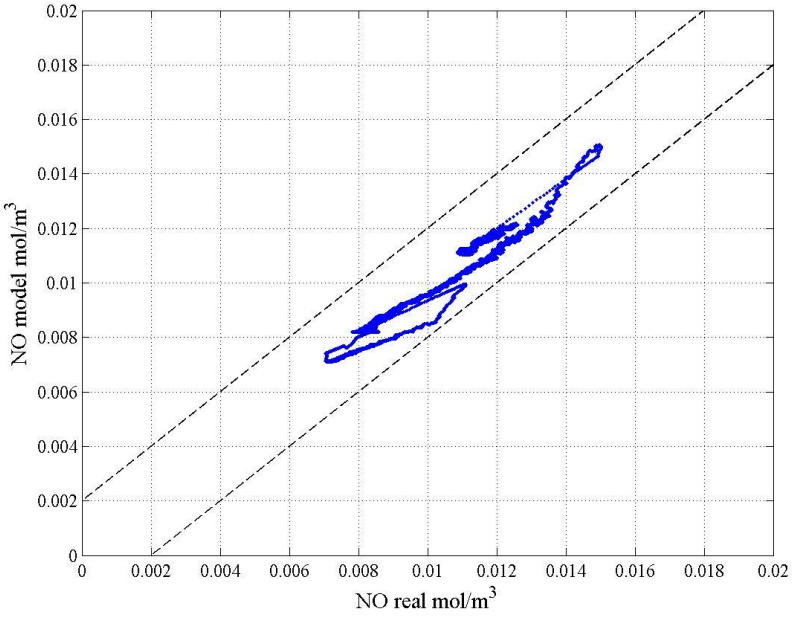

Figure 4.5. First-degree-aged DOC @1350 rpm NO model vs real.

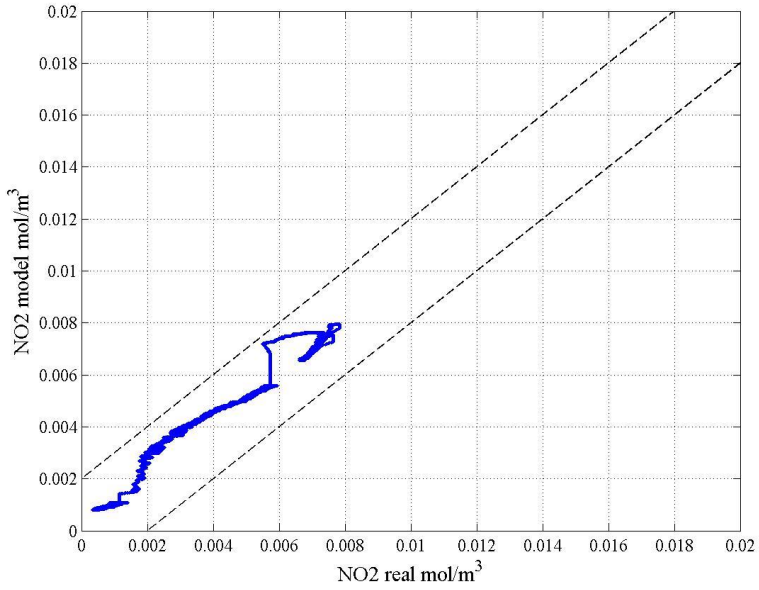

Figure 4.6. First-degree-aged DOC @1350 rpm NO model vs real.

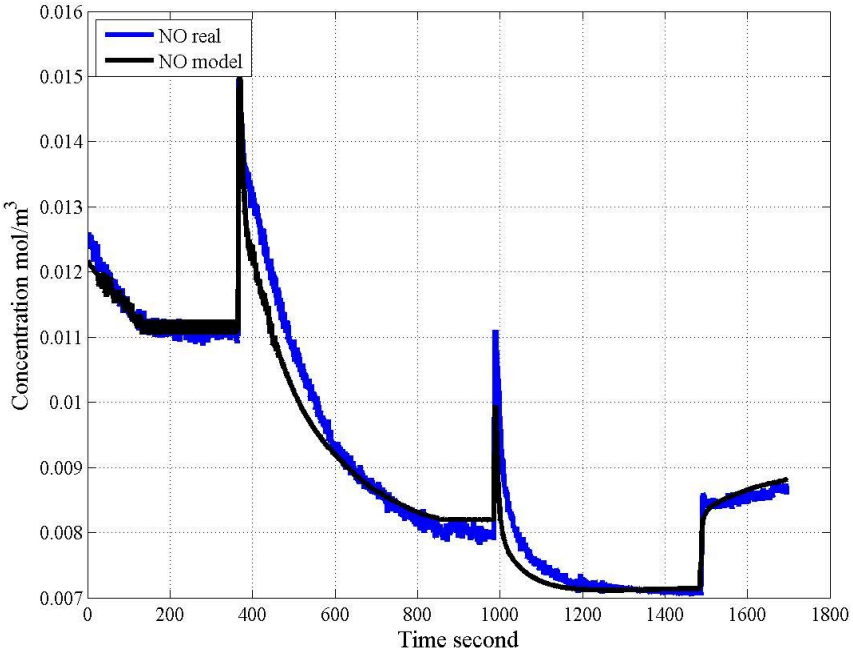

Figure 4.7. First-degree-aged DOC @1350 rpm NO real, NO model vs time.

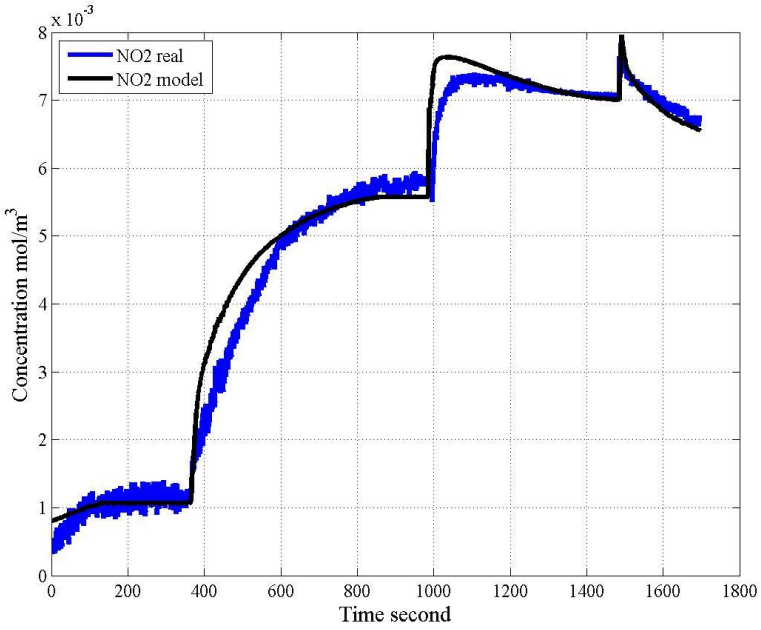

Figure 4.8. First-degree-aged DOC @1350 rpm NO real, NO model vs time.

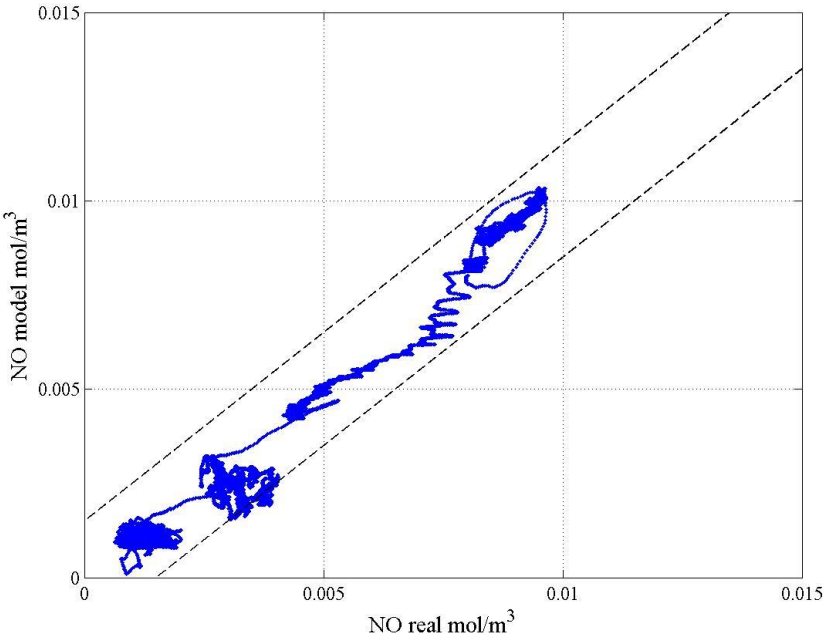

Figure 4.9. First-degree-aged DOC @1500 rpm NO model vs real.

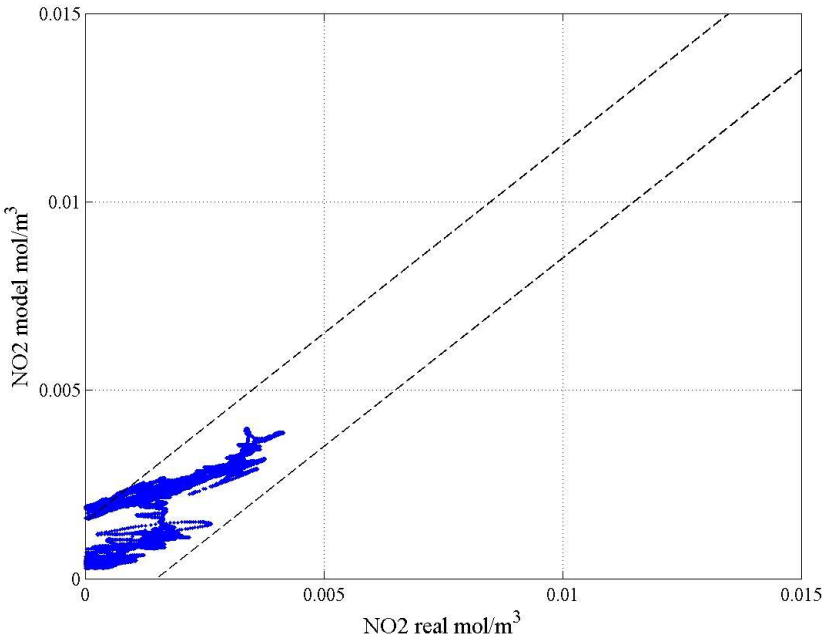

Figure 4.10. First-degree-aged DOC @1500 rpm NO_2 model vs real.

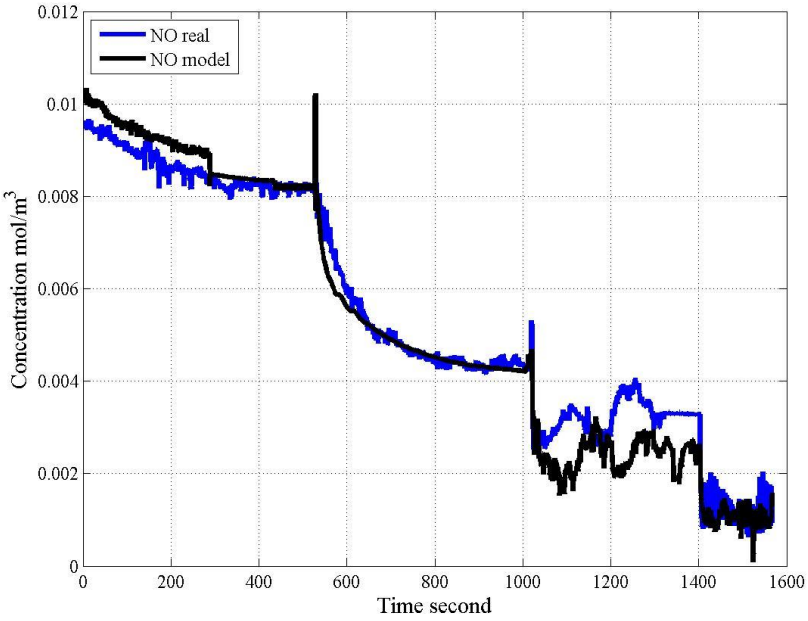

Figure 4.11. First-degree-aged DOC @1500 rpm NO real, NO model vs time.

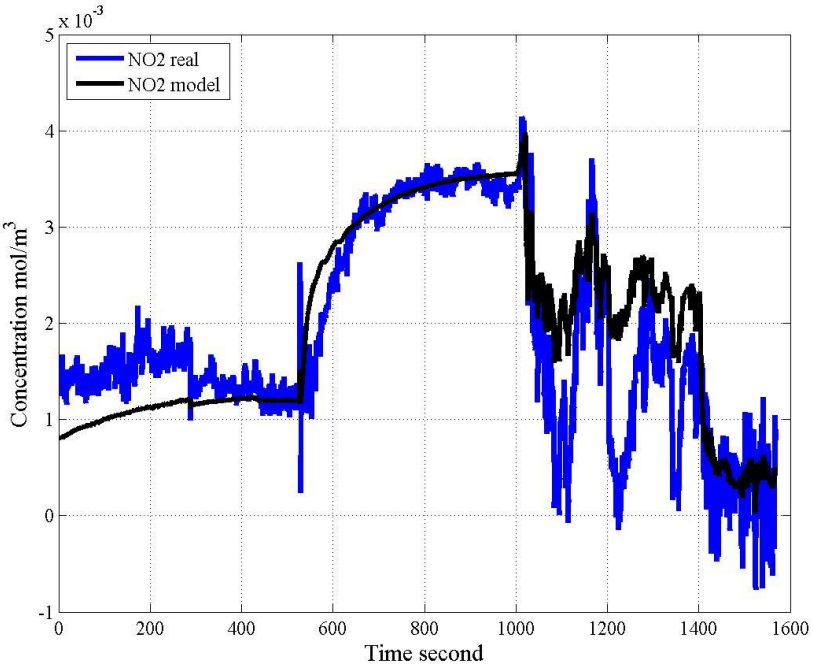

Figure 4.12. First-degree-aged DOC @1500 rpm NO_2 real, and model vs time.

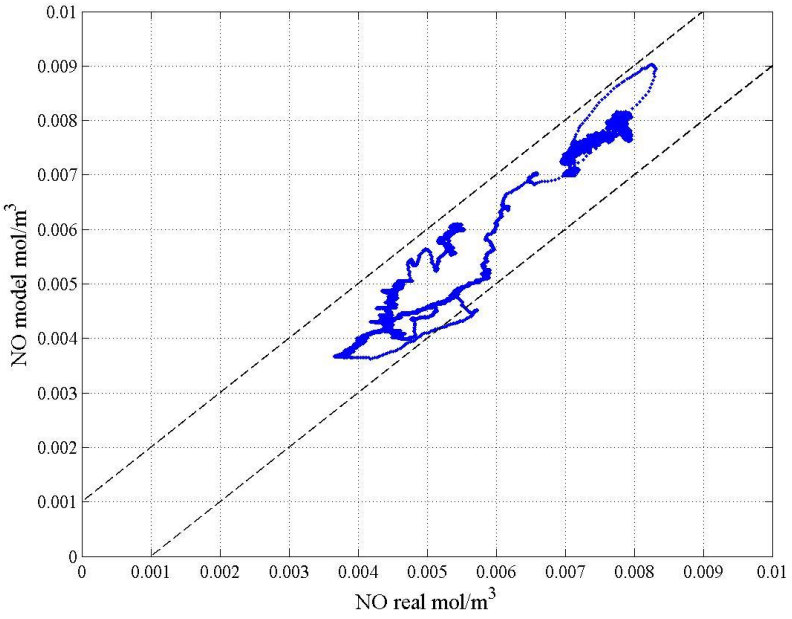

Figure 4.13. First-degree-aged DOC @1650 rpm NO model vs real.

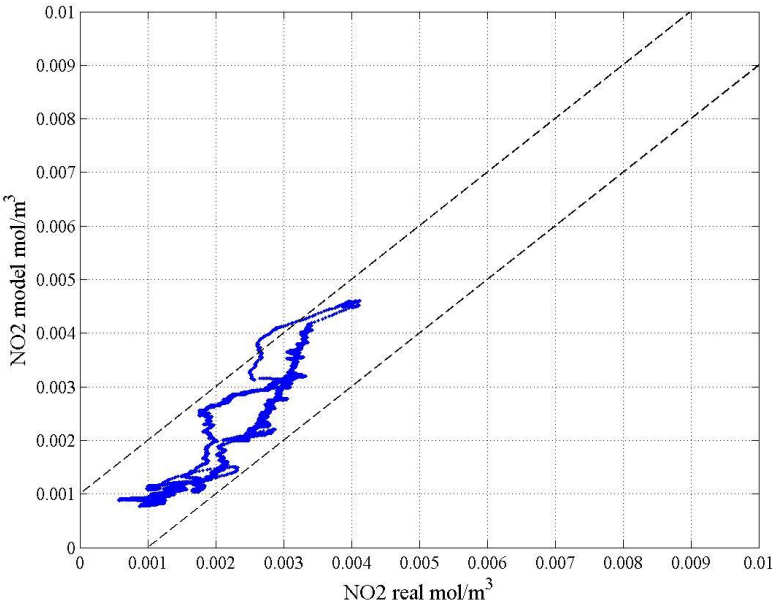

Figure 4.14. First-degree-aged DOC @1650 rpm NO_2 model vs real.

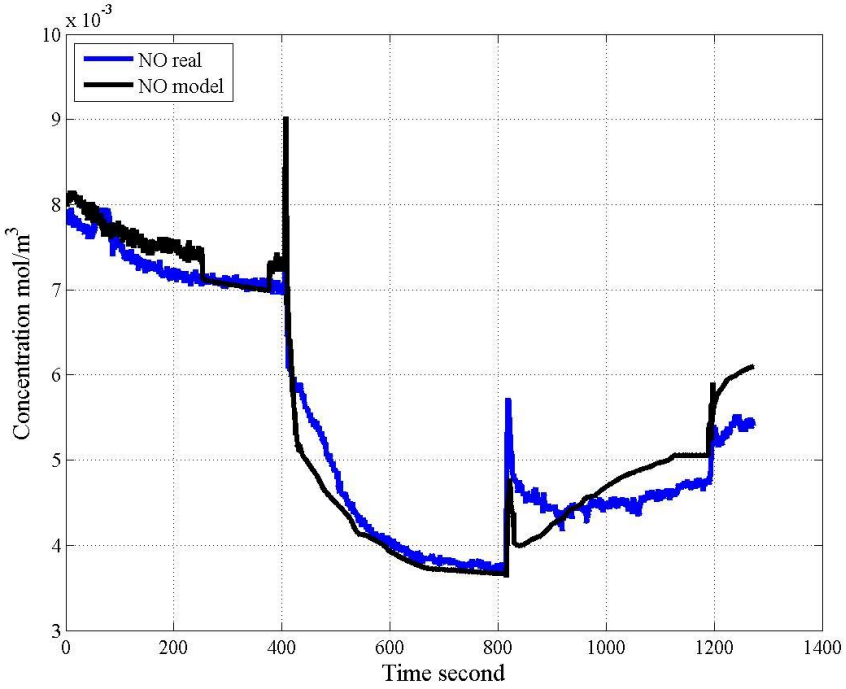

Figure 4.15. First-degree-aged DOC @1650 rpm NO real, NO model vs time.

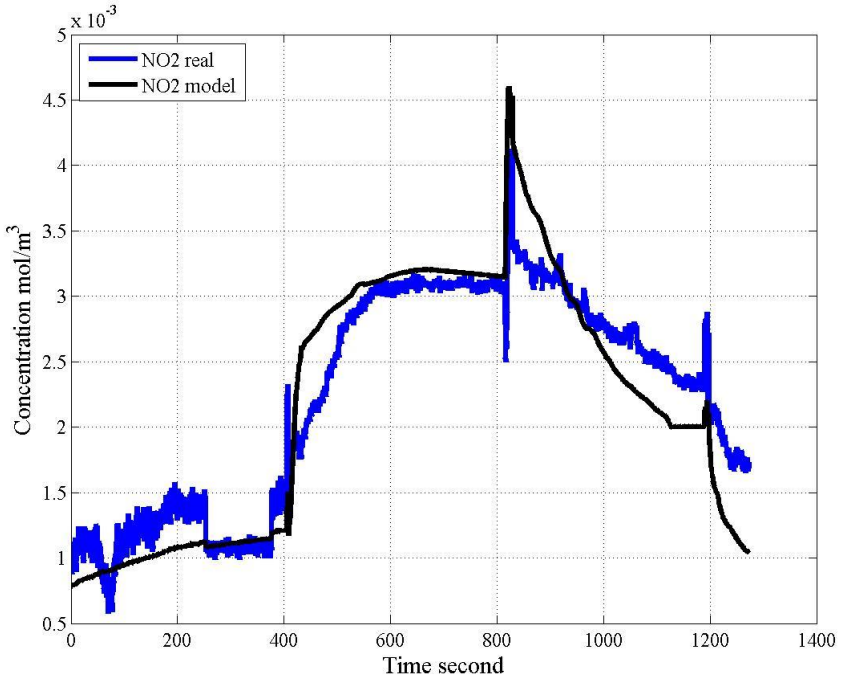

Figure 4.16. First-degree-aged DOC @1650 rpm NO_2 real, and model vs time.

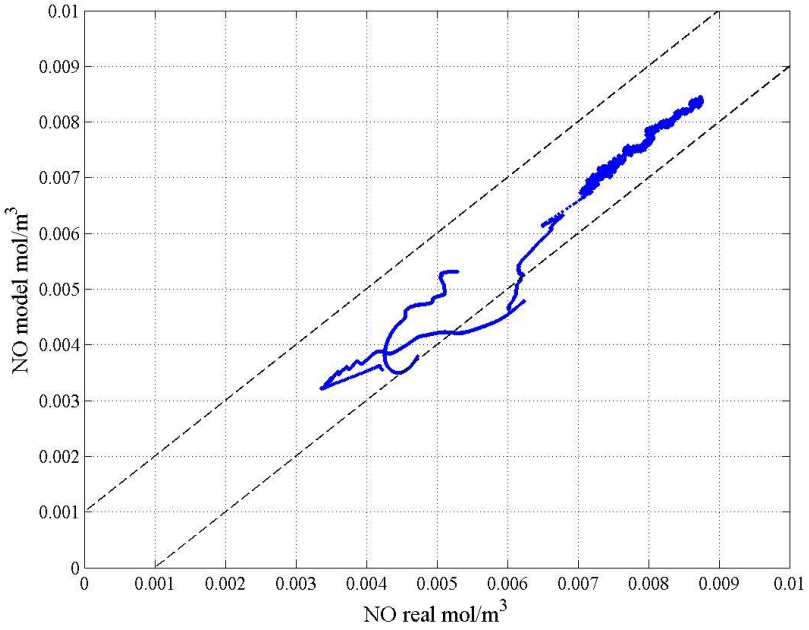

Figure 4.17. First-degree-aged DOC @1800 rpm NO model vs real.

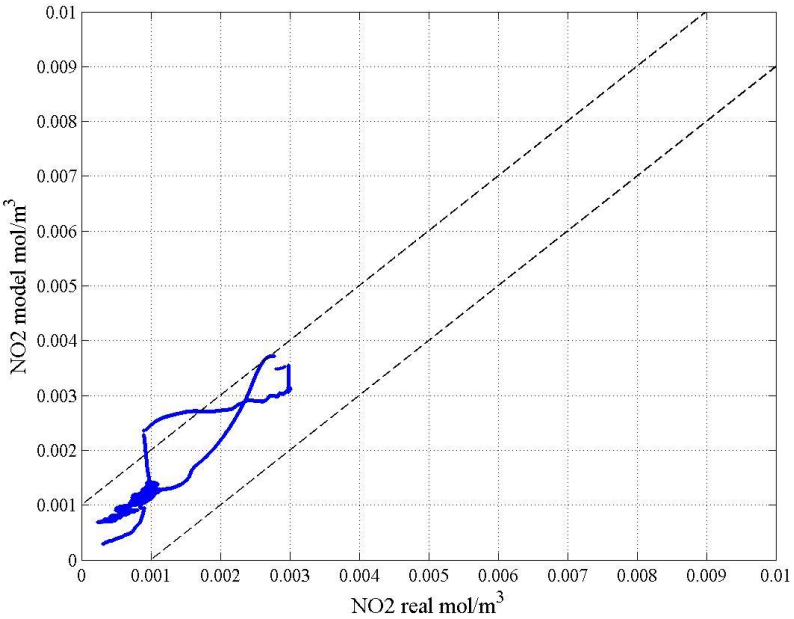

Figure 4.18. First-degree-aged DOC @1800 rpm NO_2 model vs real.

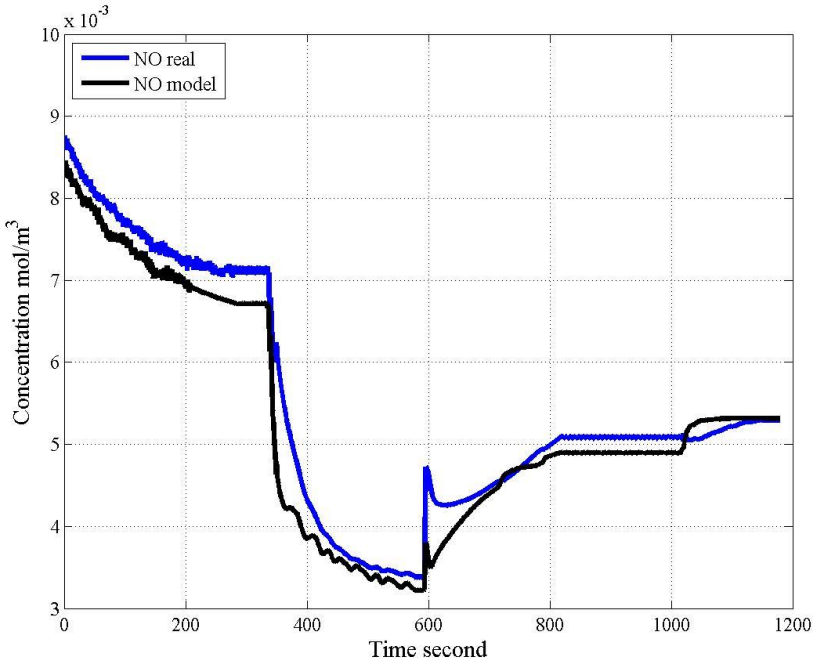

Figure 4.19. First-degree-aged DOC @1800 rpm NO real, NO model vs time.

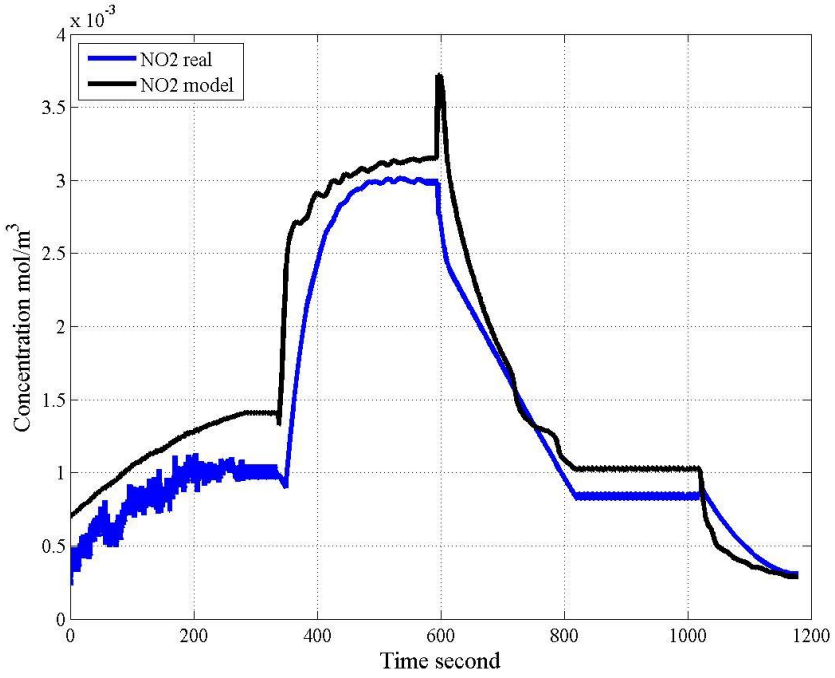

Figure 4.20. First-degree-aged DOC @1800 rpm NO_2 real, and model vs time.

4.2 Second-degree-aged DOC Experimental and Modeling Results

Table 4.2. Percentage of model points outside 10% allowance of real data.

	SPEED	NO	NO_2
Second-degree-aged DOC	1200 rpm	1.13%	1.13%
	1350 rpm	2.06%	2.06%
	1500 rpm	1.09%	1.09%
	1650 rpm	1.95%	1.95%
	1800 rpm	0.99%	0.99%

The experimental results as well as model are presented in real data vs model concentration format so that the outstanding points can be calculated numerically. As represented in the Table 4.2, aged DOC model remains an acceptable modeling result regardless of the engine speed and torque.

Figure 4.21, Figure 4.25, Figure 4.29, Figure 4.33 and Figure 4.37 show second-degree-aged DOC NO model vs real concentration at 1200, 1350, 1500, 1650 and 1800 rpm. Dashed lines are 10% error above and below y=x. Any data points outside the dashed lines are considered abnormal points, and the percentage of the abnormal points are statistically calculated and listed in Table 4.2. The largest NO model vs real concentration error occurred at 1350 rpm, which is 2.06%. This means that 2.06% modeled data points are not within 10% error of the experiment. Most of the modelled data points can reflect precisely where the real experimental points lie.

Figure 4.22, Figure 4.26, Figure 4.30, Figure 4.34 and Figure 4.38 show second-degree-aged DOC NO_2 model vs real concentration at 1200, 1350, 1500, 1650, and 1800 rpm. Similar trend can be found in NO_2 model vs real concentrations. The largest NO_2 model vs real concentrations error occurred at 1350 rpm, which is 2.06%. This means

that 2.06% modeled data points are not within 10% error of the experiment. The reason that NO_2 error is same with NO error for most cases is because real NO_2 concentration is calculated from NO_x minus NO, when NO model is abnormally higher than real data, NO_2 model at the same point will be abnormally lower than real data.

Figure 4.23, Figure 4.27, Figure 4.31, Figure 4.35 and Figure 4.39 show second-degree-aged DOC NO real and model concentrations vs time at 1200, 1350, 1500, 1650 and 1800 rpm. These figures are able to present clearly how DOC out NO concentrations change with time. If we compare NO concentration to Figure 4.3, Figure 4.7, Figure 4.11, Figure 4.15 and Figure 4.19, it can be found that at the same speed and torque condition, the NO concentration is higher in the second-degree-aged DOC. This is because after thermal aging, the DOC effectiveness level decreases, so that the amount of NO upstream getting oxidized is less in the second-degree-aged case.

Similarly, Figure 4.24, Figure 4.28, Figure 4.32, Figure 4.36 and Figure 4.40 show second-degree-aged DOC NO_2 real and model concentrations vs time at 1200, 1350, 1500, 1650 and 1800 rpm. These figures are able to present clearly how DOC-out NO_2 concentrations change with time. Because of the reduction of effectiveness of the oxidation catalyst, NO_2 concentration in second-degree-aged DOC at the same speed and torque engine condition is less than Figure 4.3, Figure 4.7, Figure 4.11, Figure 4.15 and Figure 4.19, which present the first-degree-aged case.

Interestingly, in Figure 4.31, it shows that there is quite a bit of fluctuation in NO level during the latter half of the testing. However, the model is robust enough to compensate for the fluctuation and predict the right amount of NO and NO_2 accordingly

regardless of the fluctuation of flow and torque. The reason behind the NO concentration fluctuation during steady state will be discussed later in section 4.3.

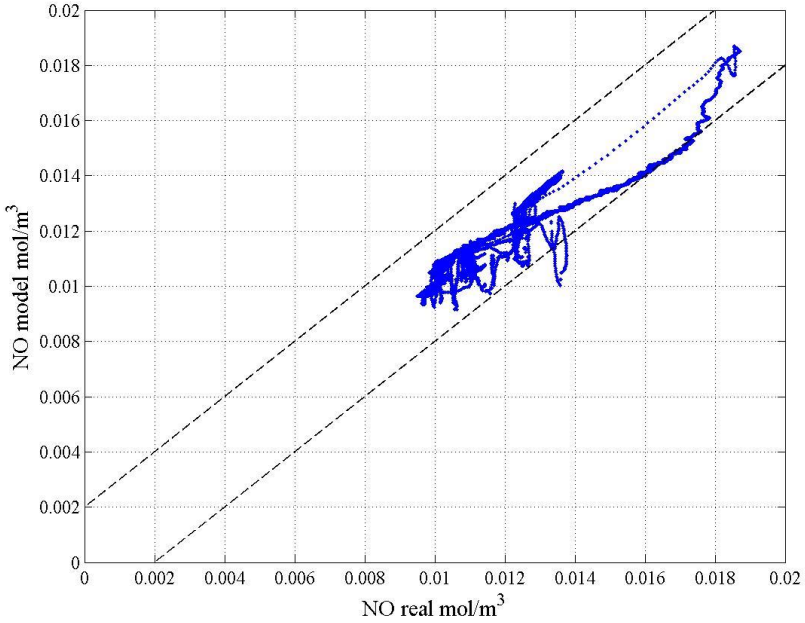

Figure 4.21. Second-degree-aged DOC @1200 rpm NO model vs real.

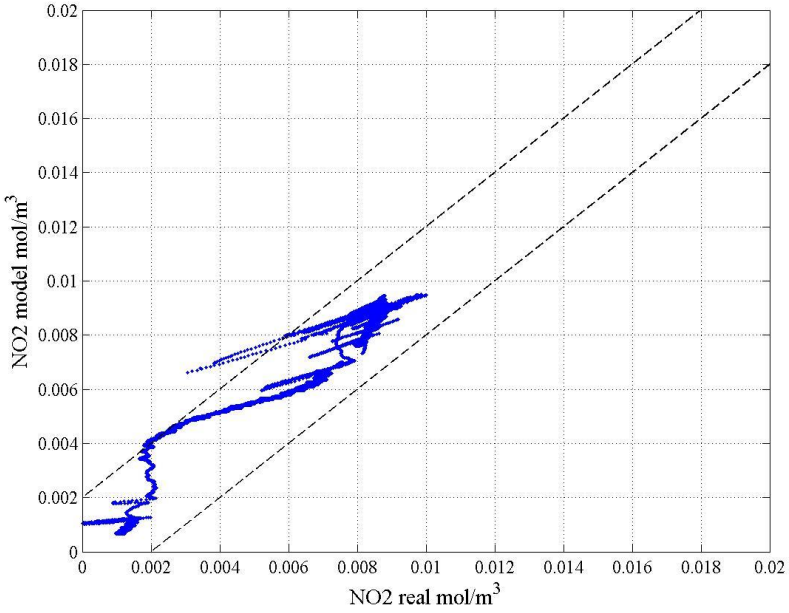

Figure 4.22. Second degree aged DOC @1200 rpm NO_2 model vs real.

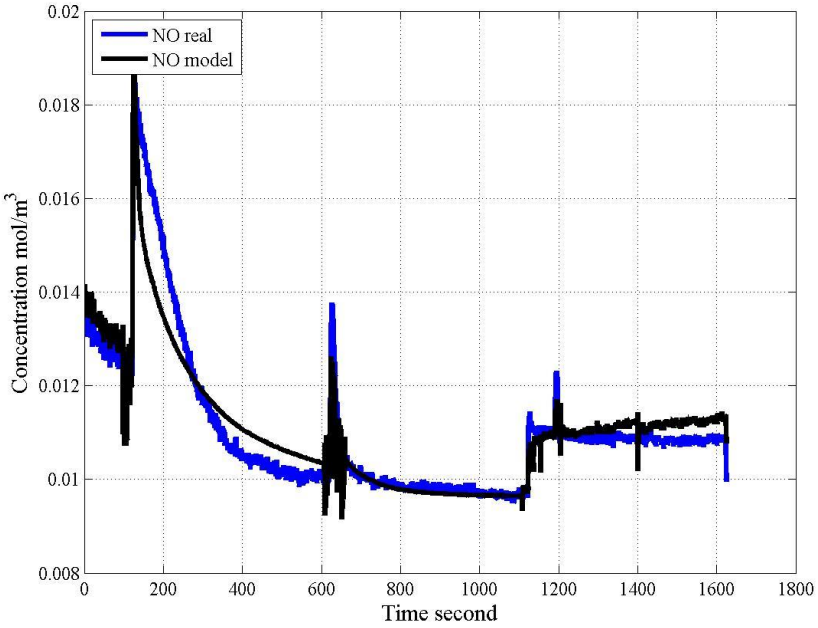

Figure 4.23. Second-degree-aged DOC @1200 rpm NO real, NO model vs time.

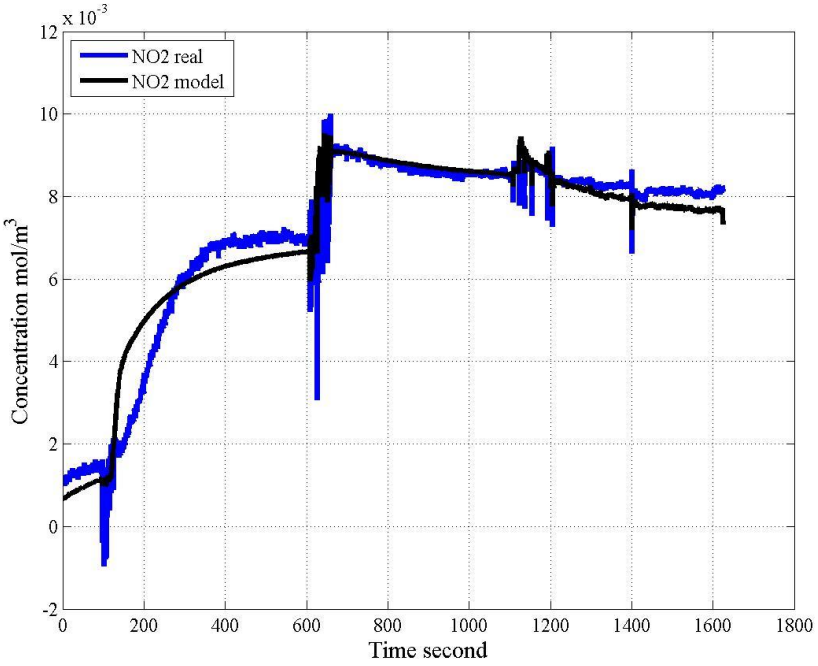

Figure 4.24. Second-degree-aged DOC @1200 rpm NO_2 real, and model vs time.

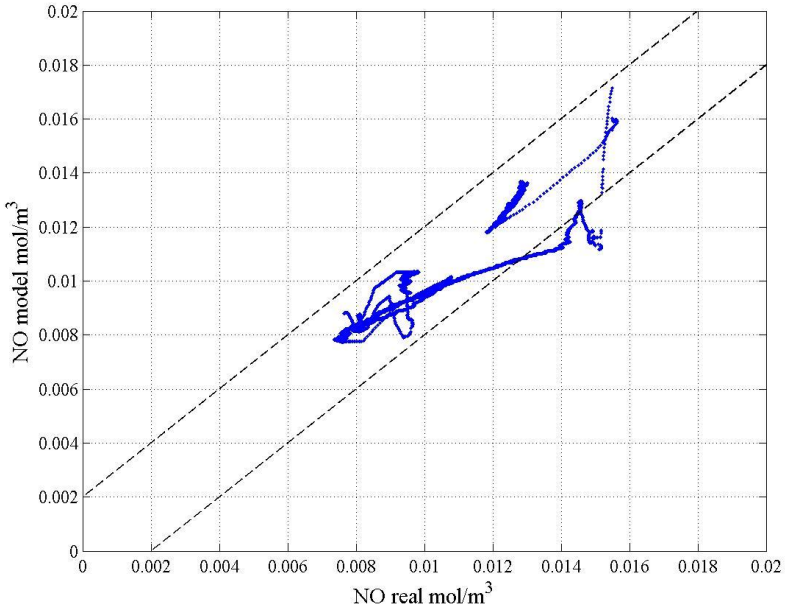

Figure 4.25. Second-degree-aged DOC @1350 rpm NO model vs real.

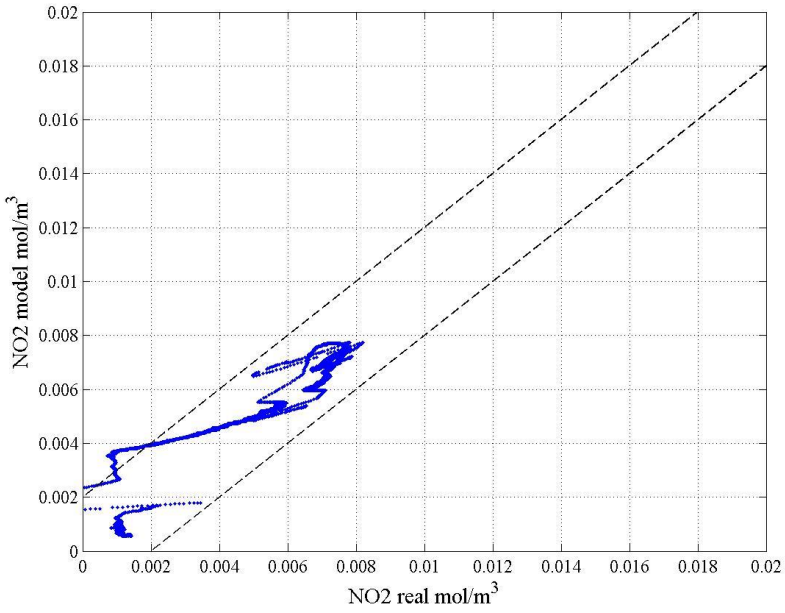

Figure 4.26. Second-degree-aged DOC @1350 rpm NO_2 model vs real.

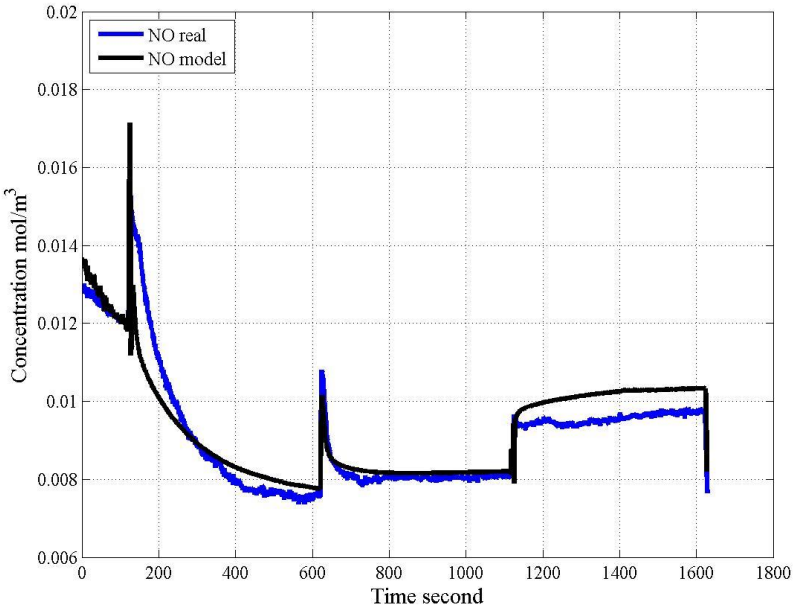

Figure 4.27. Second-degree-aged DOC @1350 rpm NO real, NO model vs time.

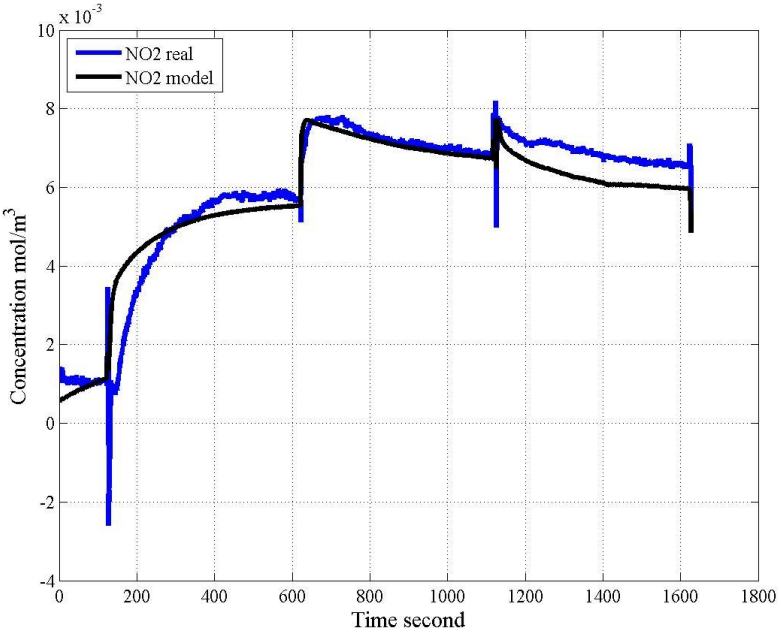

Figure 4.28. Second-degree-aged DOC @1350 rpm NO_2 real, and model vs time.

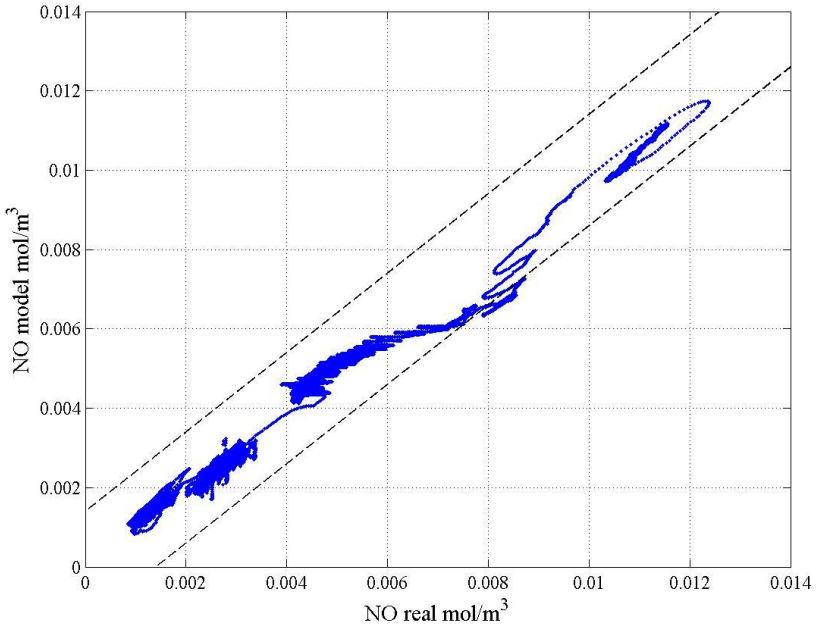

Figure 4.29. Second-degree-aged DOC @1500 rpm NO model vs real.

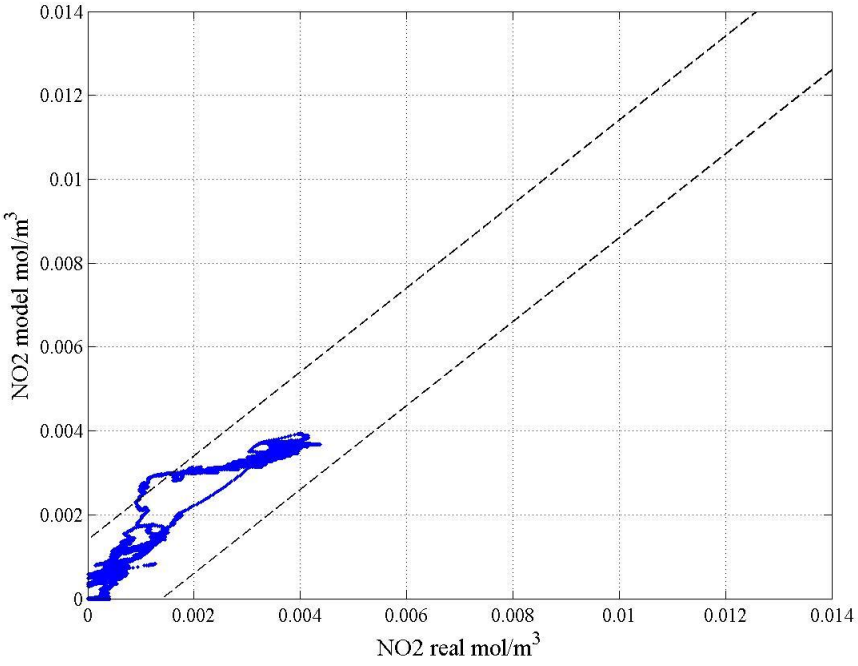

Figure 4.30. Second-degree-aged DOC @1500 rpm NO_2 model vs real.

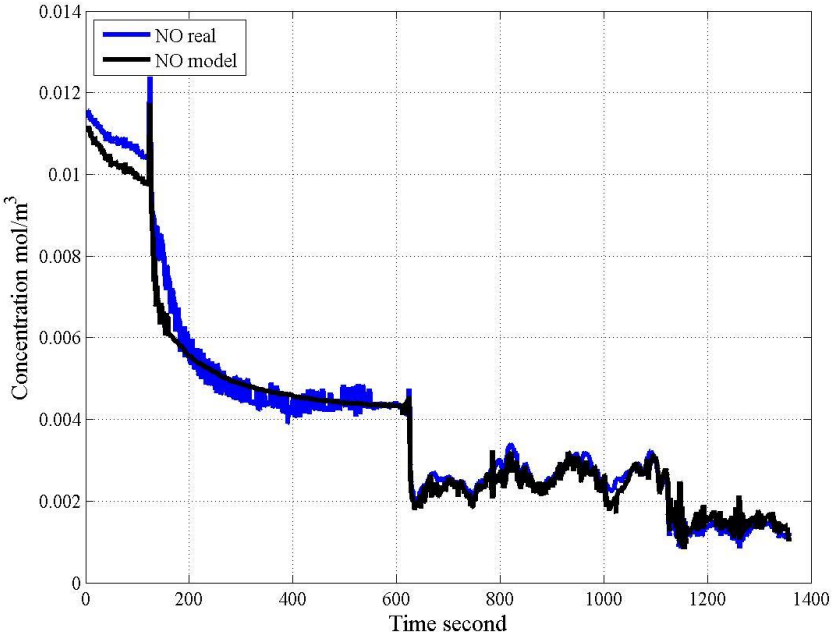

Figure 4.31. Second-degree-aged DOC @1500 rpm NO real, NO model vs time.

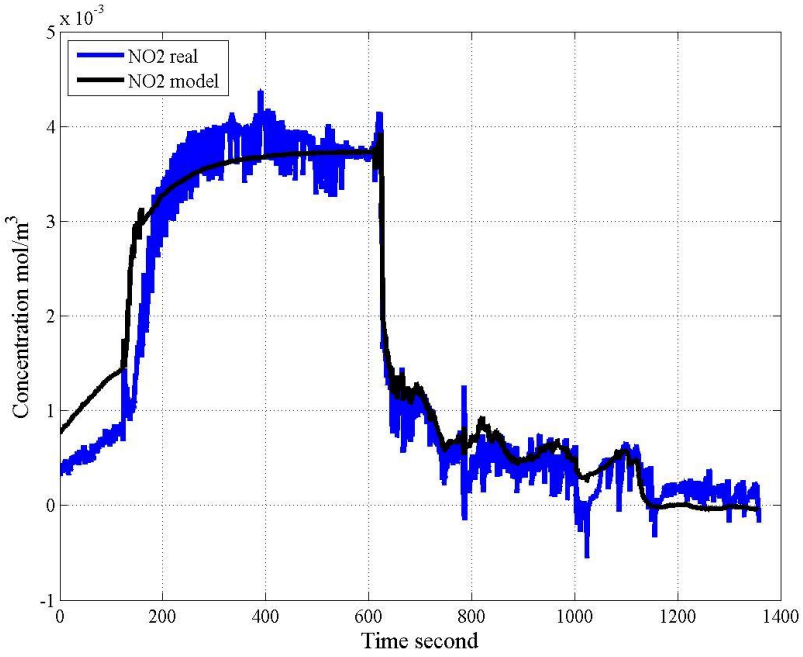

Figure 4.32. Second-degree-aged DOC @1500 rpm NO_2 real, and model vs time.

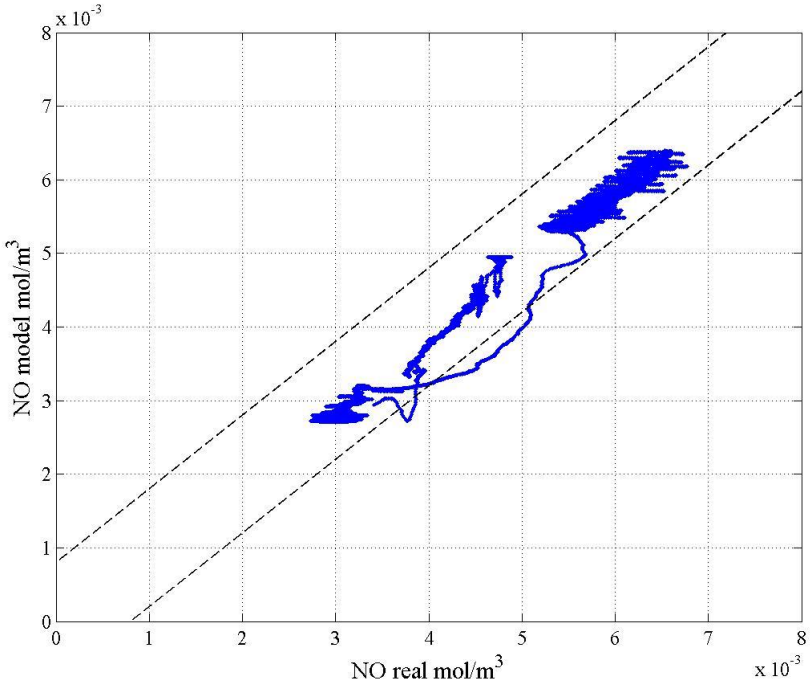

Figure 4.33. Second-degree-aged DOC @1650 rpm NO model vs real.

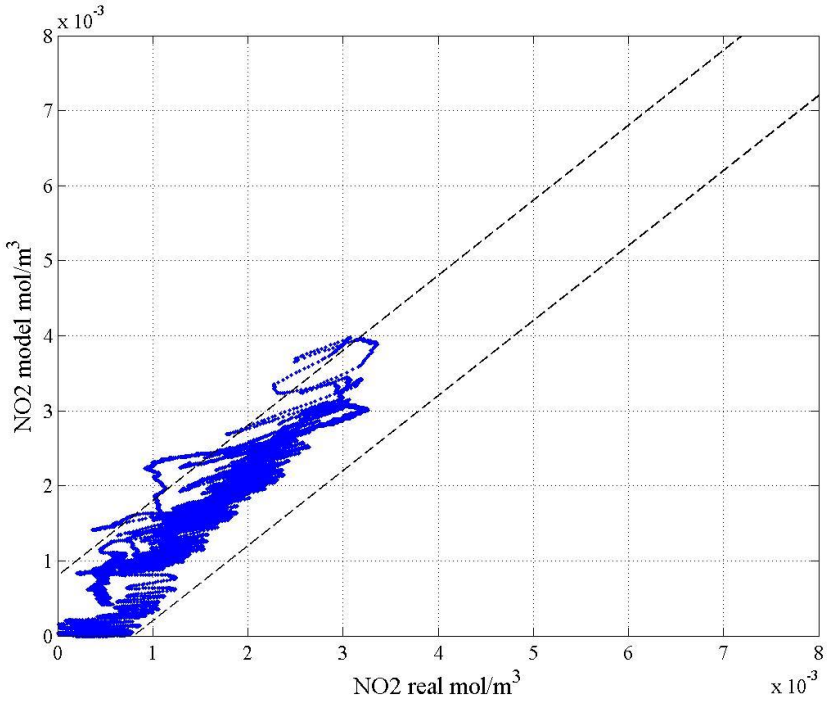

Figure 4.34. Second-degree-aged DOC @1650 rpm NO_2 model vs real.

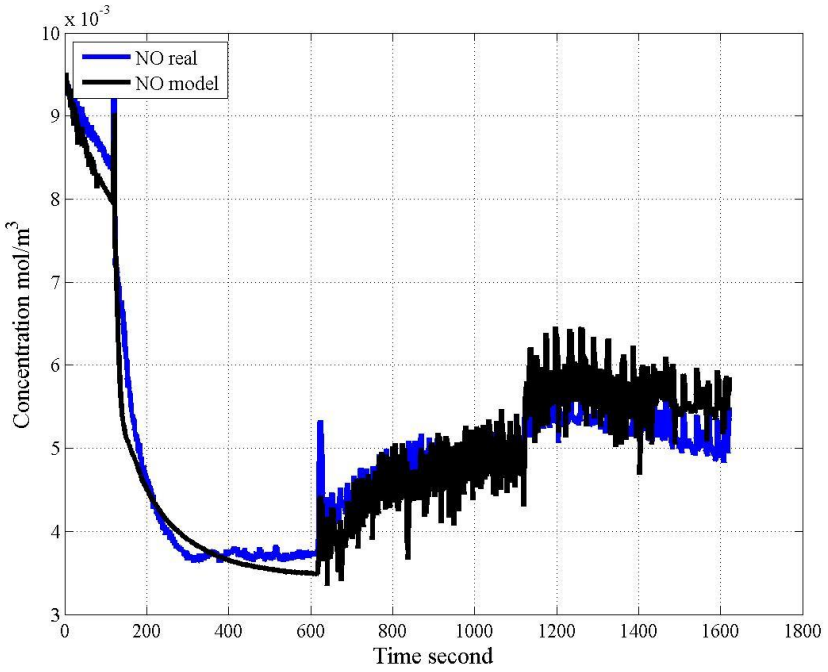

Figure 4.35. Second-degree-aged DOC @1650 rpm NO real, NO model vs time.

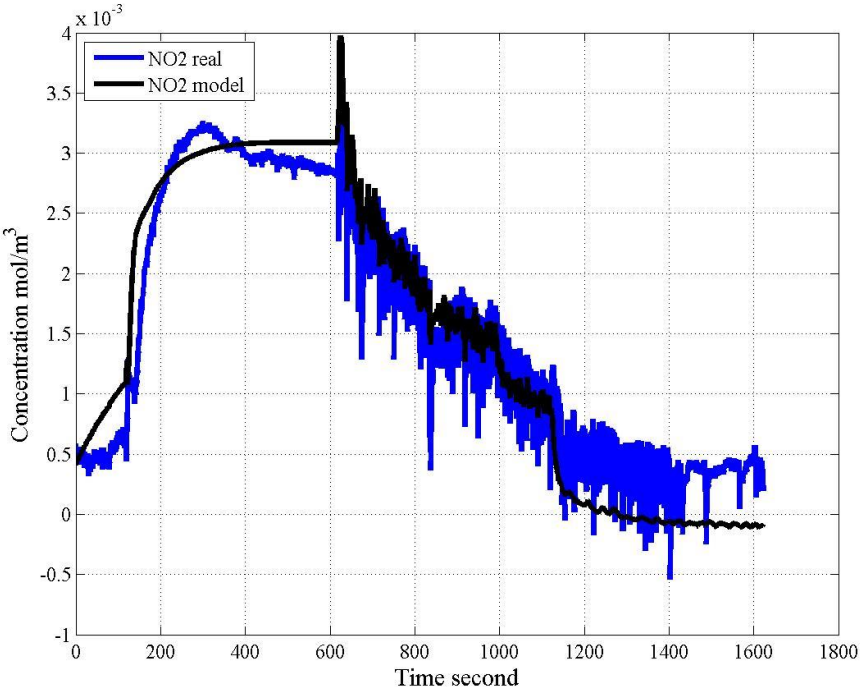

Figure 4.36. Second-degree-aged DOC @1650 rpm NO_2 real, and model vs time.

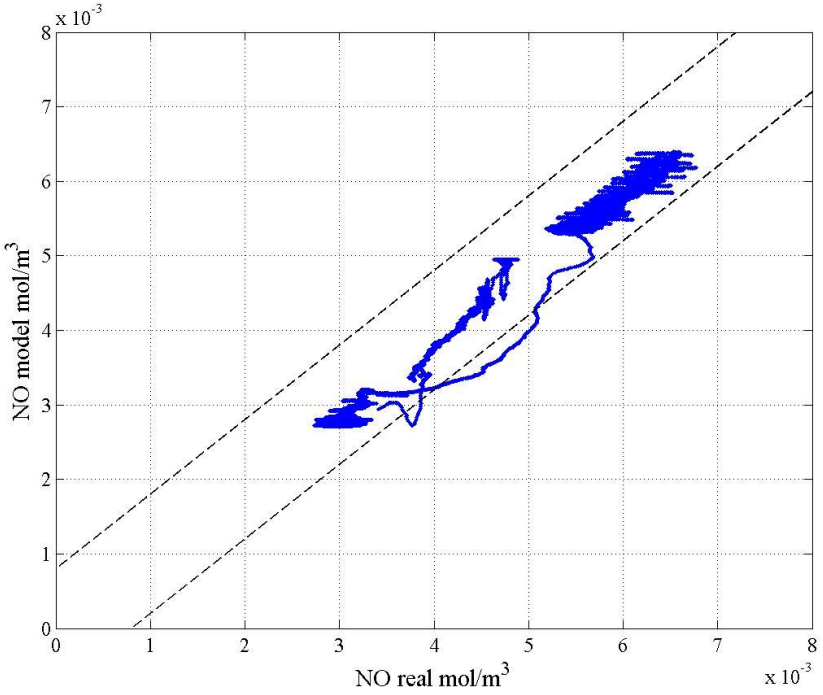

Figure 4.37. Second-degree-aged DOC @1800 rpm NO model vs real.

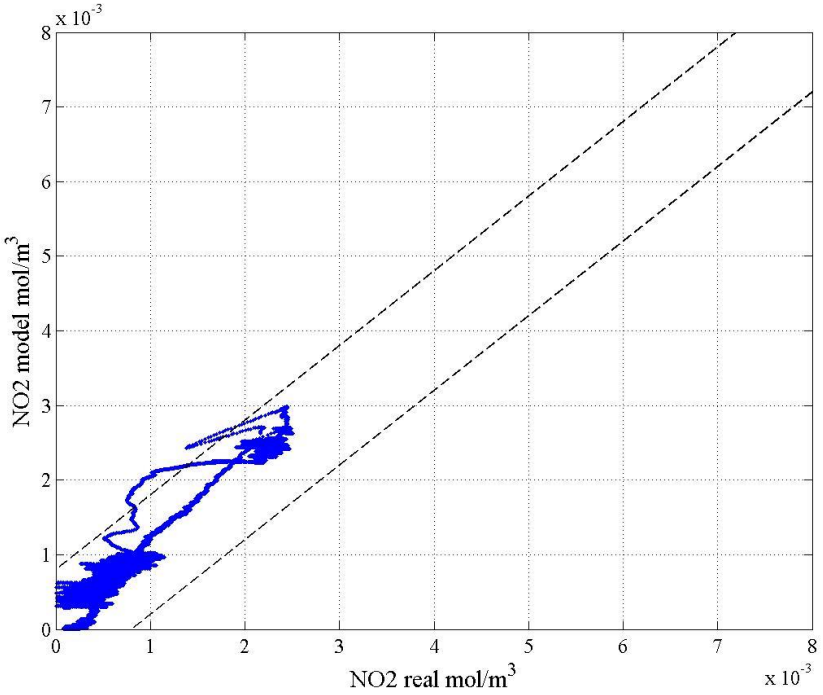

Figure 4.38. Second-degree-aged DOC @1800 rpm NO_2 model vs real.

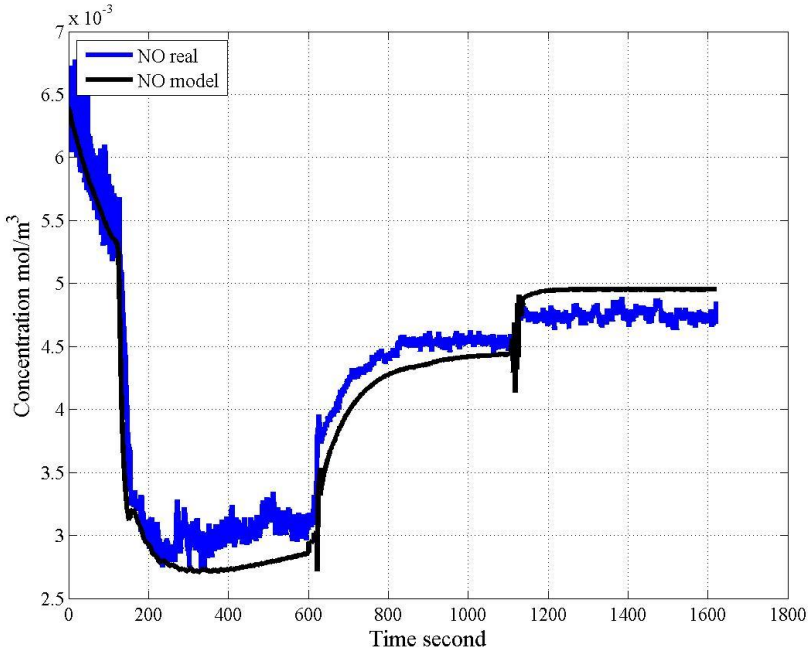

Figure 4.39. Second-degree-aged DOC @1650 rpm NO real, NO model vs time.

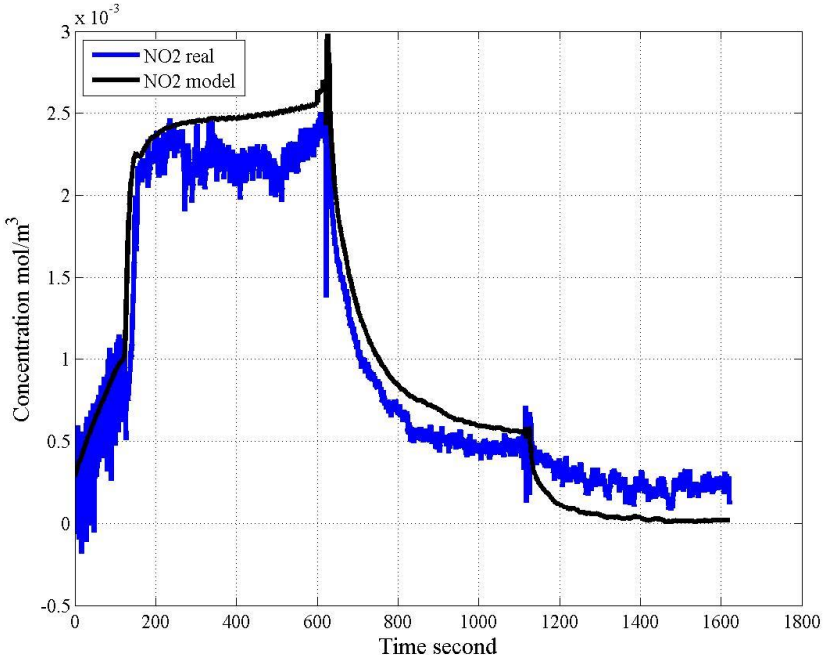

Figure 4.40. Second-degree-aged DOC @1800 rpm NO_2 real, and model vs time.

4.3 Robustness and Fluctuation Investigation in Certain Set Points

During the experiment, it was discovered that at 1500 rpm and 1650 rpm considerable abnormal fluctuations and roughness occur during signal measurement. To determine the reason behind such phenomenon, the charge flow rate and torque were plotted on the same plot of NO measurement as shown in Figure 4.41 and Figure 4.42. It is clear that the fluctuation of flow rate and torque matches the fluctuation of NO roughness, which suggests that it might be the combination of flow rate and torque fluctuation that affects the concentration of NO in diesel emission.

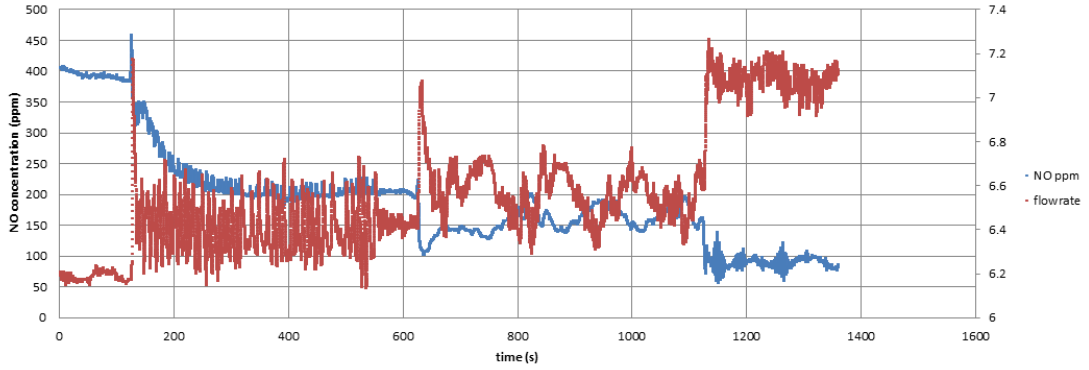

Figure 4.41. Second-degree-aged DOC @1500 rpm NO, flow vs time.

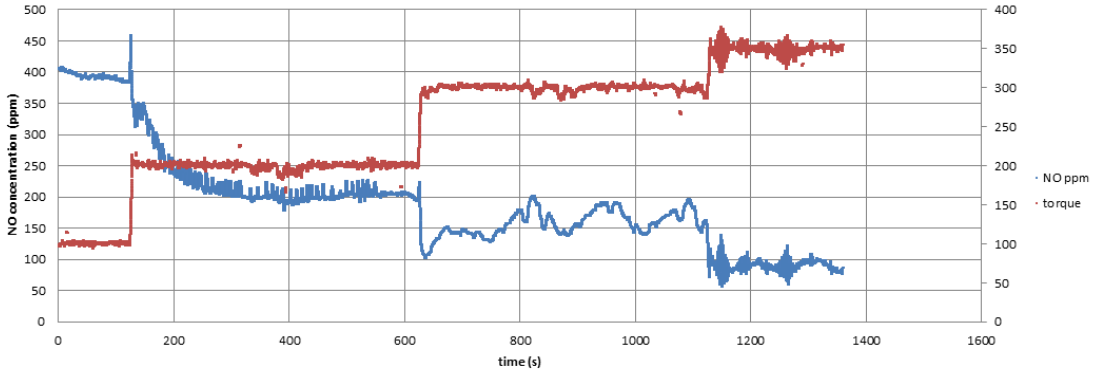

Figure 4.42. Second-degree-aged DOC @1500 rpm NO, torque vs time.

To further prove this hypothesis that flow fluctuation and torque fluctuation during steady state may result in the fluctuation and roughness of NO data, another set

point was plotted as shown in Figure 4.43 and Figure 4.44. In the 1200 rpm case, engine torque and speed are comparatively smooth. Accordingly, it is witnessed that the NO concentration during the experiment measurement is smooth too. This further proves the hypothesis that at 1500 and 1650 rpm, the fluctuation of flow rate and torque resulted in the roughness of NO and NO_x concentration measurements.

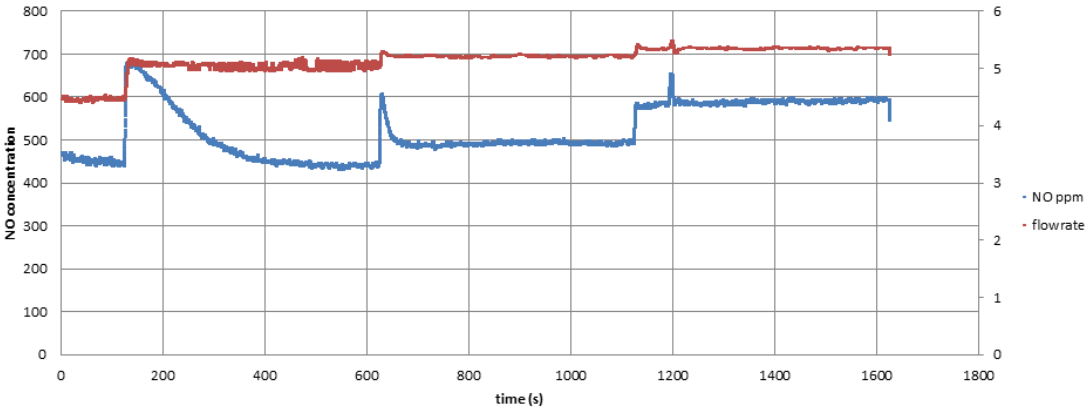

Figure 4.43. Second-degree-aged DOC @1200 rpm NO, flow vs time.

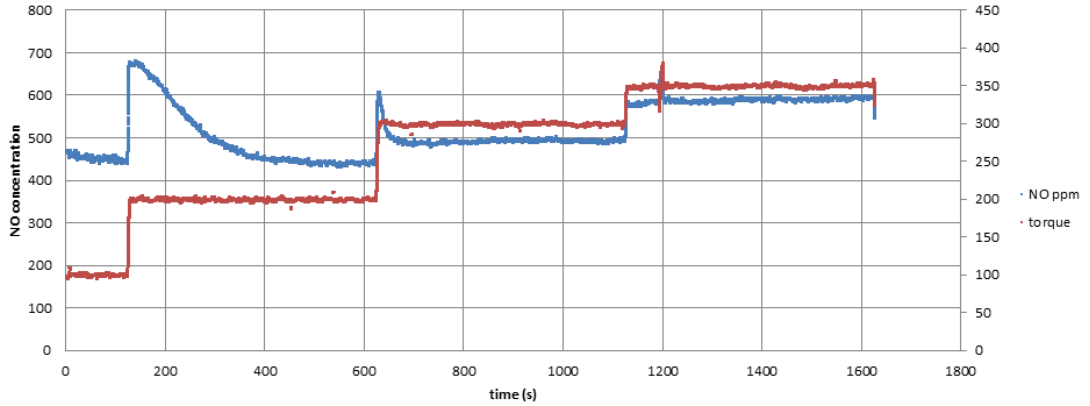

Figure 4.44. Second-degree-aged DOC @1200 rpm NO, torque vs time.

4.4 Moving Average

This section discusses the moving average and other processing techniques applied to the data. All data are measured with emission analyzers and stored in dSpace in .mat format. Moving average is applied to each measurement required for the model;

Figure 4.45 shows the DOC-out NO concentration measurement. It can be seen that there isn't too much noise signal in the NO concentration measurement. However, the moving average in the period of 30 is able to smooth out the signal into better performance without aliasing. Figure 4.46 shows the DOC out NO_x concentration measurement. Unlike the measurement of NO, NO_x signal contains high frequency noise. Also, due to the structural and conversion theory of NO_x analyzer, NO_x measurement is much noisier. Moving average is able to smooth out partially high frequency noise, but moving average alone is not able to smooth out NO_x signal.

Figure 4.47 shows the secondary data processing for NO_x data. Unlike NO which is oxidized through the DOC, NO_x data at constant torque, speed, and flow rate condition remains constant. Here, concentration at each torque is averaged out and forced constant at each setpoint. The Averaged NO_x concentration is able to represent the normal operation condition for NO_x concentration.

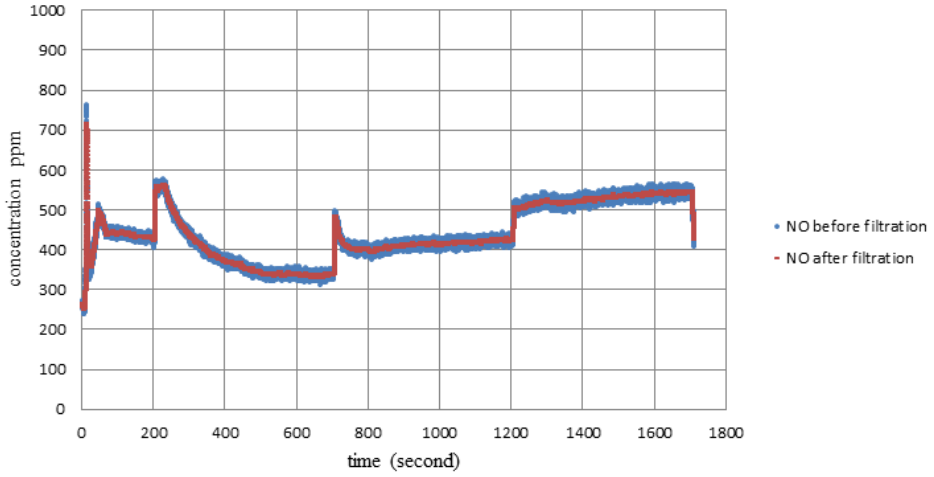

Figure 4.45. DOC out NO concentration measurement and averaging.

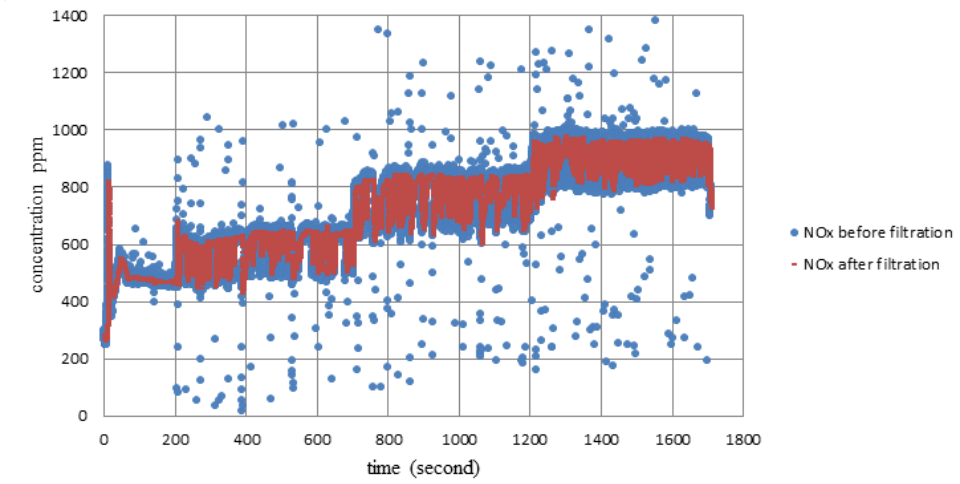

Figure 4.46. DOC out NO_x concentration measurement and averaging.

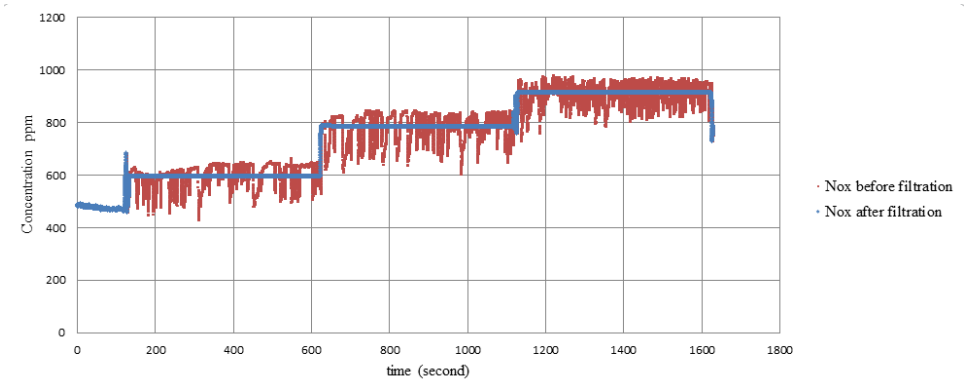

Figure 4.47. DOC out NO_x concentration secondary averaging

4.5 Oxygen Concentration in Engine Emission Recalculation

In hybrid modeling discussed in section 3.2, it was explained that since there is no oxygen sensor available in aftertreatment setup, oxygen concentration was kept 19% by volume in calibration. However, in actual practice, the air-fuel ratio varies depending on engine speed and torque. When the engine is idling, the emission oxygen can be as lean as fresh air, while during high load conditions, the emission can be as rich as only 5% by volume concentration of oxygen. In order to specify different cases and specialize the

oxygen concentration in each case, fueling and fresh air flow measurements were taken into account in the equation of :

$$C_3H_6 + 4.5O_2 \xrightarrow{combustion} 3CO_2 + 3H_2O \quad (4.1),$$

and the emission oxygen concentration by volume percentage is listed in Table 4.3.

Table 4.3 Engine out oxygen concentration in different setpoints.

	1200 rpm	1350 rpm	1500 rpm	1650 rpm	1800 rpm
100 lb-ft	19.910%	19.985%	20.039%	19.993%	19.653%
200 lb-ft	19.344%	19.414%	19.293%	19.240%	19.158%
300 lb-ft	18.853%	18.903%	18.820%	18.775%	18.717%
350 lb-ft	18.411%	18.512%	18.517%	18.677%	18.517%

From above investigation, engine out oxygen by volume from experimental setpoints are about 19.137% by volume. Largest oxygen concentration occurs at 1500 rpm, 100 lb-ft setpoint, while the smallest oxygen concentration occurs at 1200 rpm, 350 lb-ft. The biggest oxygen concentration difference in engine out will result in maximum difference of Kp of 4.08%.

Oxygen consumption through DOC is also analyzed. In all cases HC getting oxidized is less than 300 ppm, CO concentration less than 50 ppm, NO concentration less than 700 ppm. In this maximum consumption case of oxygen, 1300 ppm of oxygen will be involved in oxidation reaction, which will result in 0.13% oxygen difference between DOC inlet and DOC outlet. Thus oxidation through DOC will not cause big enough error to result in imprecision in the model.

After the discussion above, it can be concluded that calculated engine out oxygen in Table 4.3 is able to estimate oxygen concentration as DOC out oxygen concentration. Modeling of Kp will keep oxygen concentration as 19% by volume.

CHAPTER 5. CONCLUSION AND FUTURE WORK

5.1 Conclusions

Experiments on first-degree aged DOC have been performed. 1200, 1350, 1500, 1650 and 1800 rpm of speed and 100, 200 300 and 350 lb-ft of torque are chosen as setpoints for experiments. Upstream and downstream of DOC HC, NO, and NO_x concentrations have been measured and processed. Experiments have been conducted multiple times and the repeatability and reliability of the measurement have been confirmed.

A model of Kp as a function of DOC temperature is calibrated upon first-degree-aged DOC experimental data. Comparison and analysis have been conducted. It has been observed that, at most setpoints, Kp model is proved to be able to predict precisely the downstream NO and NO_2 concentrations. Abnormal test points have been analyzed and the fluctuation in emission concentration was found to be connected with the issue internal to the charge flow control as well as torque control.

Thermal aging has been performed on the diesel oxidation catalyst, and second-degree aged DOC experiments have been performed. 1200, 1350, 1500, 1650 and 1800 rpm of speed and 100, 200 300 and 350 lb-ft of torque are chosen as setpoints for experiments. Upstream and downstream DOC HC, downstream DOC NO and NO_x concentrations have been measured and processed. Experiments have been conducted

twice and the repeatability and reliability of the measurement have been confirmed. Kp model has been recalibrated to the second-degree-aged DOC and experimental downstream DOC NO and NO_2 concentrations have been analyzed and compared with the modelled data. It has been proved that statistically the model is able to give good predictions.

Compared with other DOC-out NO and NO_2 modeling methods, this model requires less effort in calibrating parameters regarding to chemical reaction. Also, fewer inputs are required to model the downstream DOC NO and NO_2 concentrations.

HC light-off temperature has been calculated through direct measurement and 70 K of light-off temperature shift is achieved through the process of aging. A preliminary 3-D model of Kp which predicts the downstream DOC NO and NO_2 concentration as a function of total NO_x, DOC temperature, and HC light-off temperature has been built and presented.

5.2 Future Work

To finally accomplish the goal of predicting downstream NO/NO_2 ratio only with DOC temperature profile, it requires modeling the HC light-off temperature. This part of the research has already been analyzed by Sutjiono [6]. However second-degree-aged DOC light-off temperature shift still requires calibration.

As mentioned earlier, current modeling treats oxygen concentration downstream DOC as 19% by volume. Measurement of oxygen or calculation of oxygen concentration through direct measurement is required to recalibrate the model for a more precise oxygen concentration input of the model.

Further proof that DOC deactivation has the same impact on different species will be useful for further research, since the fundamental idea behind this research is to model the NO/NO_2 ratio shift by capturing HC light-off temperature shift. Further investigation need to be conducted regarding the selectivity of the catalyst and whether catalyst aging has the same impact on reducing the rate of reaction for both species.

More levels of thermal aging need to be conducted in the future for further calibration. Since currently only first-degree-aged DOC and second-degree-aged DOC have been calibrated and analyzed, more levels of aging requires seeing if the further aged DOC experimental data and model will still be consistent.

LIST OF REFERENCES

LIST OF REFERENCES

[1] http://www.dieselnet.com/standards/us/hd.php

[2] Konstandopoulos, Athanasios G., and John H. Johnson. "Wall-Flow Diesel Particulate Filters their Pressure Drop and Collection Efficiency." Training 2013 (1989): 11-11.

[3] Konstandopoulos, Athanasios G., et al. "Fundamental studies of diesel particulate filters: transient loading, regeneration and aging." SAE technical paper (2000): 01-1016.

[4] Huynh, Cuong T., et al. "A one-dimensional computational model for studying the filtration and regeneration characteristics of a catalyzed wall-flow diesel particulate filter." SAE transactions 112.4 (2003): 620-646

[5] Schultz, Ryan, and Peter Meckl. "Degradation of Nonmethane Hydrocarbon Oxidation Efficiency of a Catalyzed Diesel Particulate Filter during Aging." SAE International Journal of Engines 4.1 (2011): 1776-1783.

[6] Sutjiono, Raymond, et al. "Real-Time On-Board Indirect Light-Off Temperature Estimation as a Detection Technique of Diesel Oxidation Catalyst Effectiveness Level." Training 2013: 11-04.

[7] Ransome-Wallis, Patrick, ed. Illustrated Encyclopedia of World Railway Locomotives. Courier Dover Publications, 2012.

[8] McNeil, Ian, ed. Encyclopaedia of the History of Technology. Routledge, 2002.

[9] Wrangham, D.A. (1956). The Theory & Practice of Heat Engines. Cambridge University Press. p. 664.

[10] Hooley, Ray E. "Sparks and Flames: Ignition in Engines--An Historical Approach." (1999): 687-688.

[11] Bryant, Lynwood. "The development of the diesel engine." Technology and Culture (1976): 432-446.

[12] Katare, Santhoji R., Joseph E. Patterson, and Paul M. Laing. "Diesel aftertreatment modeling: A systems approach to NO x control." Industrial & engineering chemistry research 46.8 (2007): 2445-2454.

[13] Palucka, Tim. "DOING THE IMPOSSIBLE Reducing auto emissions by 90 percent in a few years looked easy to Congress." AMERICAN HERITAGE OF INVENTION AND TECHNOLOGY 19.3 (2004): 22-33.

[14] Gallezot, P., et al. "Catalyst Deactivation." EE Peterson and AT Bell, Eds(1987): 263.

[15] Reitze Jr, Arnold W. "Controlling Automotive Air Pollution Through Inspection and Maintenance Programs." Geo. Wash. L. Rev. 47 (1978): 705.

[16] Stewart, Walter F. "Operating experience with a liquid-hydrogen fueled Buick and refueling system." International journal of hydrogen energy 9.6 (1984): 525-538.

[17] EPA-Diesel, R. I. A. "Regulatory impact analysis: heavy-duty engine and vehicle standards and highway diesel fuel sulfur control requirements." United States Environmental Protection Agency, Air and Radiation EPA420-R-00-026(2000).

[18] Alkordi, Mohamed H., et al. "Zeolite-like metal− organic frameworks as platforms for applications: on metalloporphyrin-based catalysts." Journal of the American Chemical Society 130.38 (2008): 12639-12641.

[19] Pfeifer, M., et al. "The second generation of catalyzed diesel particulate filter systems for passenger cars: Particulate filters with integrated oxidation catalyst function." SAE transactions 114.4 (2005): 639-651.

[20] Padilla, Antonio Triana. Development of models to study the emissions, flow, and kinetic characteristics from diesel oxidation catalysts and particulate filters. Diss. Michigan Technological University, 2005.

[21] Clerc, James C. "Catalytic diesel exhaust aftertreatment." Applied Catalysis B: Environmental 10.1 (1996): 99-115.

[22] Zinola, Stéphane, Jacques Lavy, and Anne Jaecker-Voirol. "Towards CO and HC aftertreatment devices for the next generation of diesel engines." Training2013 (2008): 12-05.

[23] Johnson, Jon E., and David B. Kittelson. "Physical factors affecting hydrocarbon oxidation in a diesel oxidation catalyst." Training 2014 (1994): 04-30.

[24] Lassi, Ulla. Deactivation correlations of Pd/Rh three-way catalysts designed for Euro IV Emission Limits: effect of ageing atmosphere, temperature and time. Oulun yliopisto, 2003.

[25] Heck, Ronald M., Robert J. Farrauto, and Suresh T. Gulati. Catalytic air pollution control: commercial technology. John Wiley & Sons, 2012.

[26] Ihara, Kazunori, Hiroshi Murakami, and Kazuko Yamagata. "Catalyst for purification of exhaust gases." U.S. Patent No. 5,075,275. 24 Dec. 1991.

[27] Suhonen, S., et al. "High-temperature-aging-promoted Rh oxides on supported automotive exhaust catalysts." Surface and interface analysis 34.1 (2002): 76-79.

[28] Bartholomew, Calvin H. "Mechanisms of catalyst deactivation." Applied Catalysis A: General 212.1 (2001): 17-60.

[29] Forzatti, Pio, and Luca Lietti. "Catalyst deactivation." Catalysis today 52.2 (1999): 165-181.

[30] Heck, Ronald M., and Robert J. Farrauto. "Automobile exhaust catalysts."Applied Catalysis A: General 221.1 (2001): 443-457.

[31] Heck, Ronald M. "Catalytic abatement of nitrogen oxides–stationary applications." Catalysis Today 53.4 (1999): 519-523.

[32] http://en.wikipedia.org/wiki/Heterogeneous_catalysis

[33] Oh, Se H., and James C. Cavendish. "Transients of monolithic catalytic converters. Response to step changes in feedstream temperature as related to controlling automobile emissions." Industrial & Engineering Chemistry Product Research and Development 21.1 (1982): 29-37.

[34] Depcik, Christopher David. Modeling Reacting Gases and Aftertreatment Devices for Internal Combustion Engines. Diss. The University of Michigan, 2003.

[35] Voltz, Sterling E., et al. "Kinetic study of carbon monoxide and propylene oxidation on platinum catalysts." Industrial & Engineering Chemistry Product Research and Development 12.4 (1973): 294-301.

[36] Hsieh, Ming-Feng, and Junmin Wang. "NO and NO_2 concentration modeling and observer-based estimation across a diesel engine aftertreatment system."Journal of Dynamic Systems, Measurement, and Control 133.4 (2011): 041005.

[37] Katare, Santhoji. "Robust Parameter Estimation Algorithms for Nonlinear Aftertreatment Models." Training 2014 (2006): 04-28.

[38] Grossale, Antonio, et al. "The chemistry of the $NO/NO_2/ NH_3$ “fast” SCR reaction over Fe-ZSM5 investigated by transient reaction analysis." Journal of Catalysis 256.2 (2008): 312-322.

[39] Chatterjee, Daniel, et al. Numerical simulation of $NO/NO_2/NH_3$ reactions on SCR-catalytic converters: model development and applications. No. 2006-01-0468. SAE Technical Paper, 2006.

[40] Usmen, R. K., et al. "Techniques for analyzing thermal deactivation of automotive catalysts." Training 2014 (1992): 03-11.